Supporting Information for

Transcriptional burst frequency and burst size are equally modulated across the human genome

Roy D. Dar[*], Brandon S. Razooky[*], Abhyudai Singh, Thomas V. Trimeloni, James M. McCollum, Chris D. Cox, Michael L. Simpson[**], Leor S. Weinberger[**]

[*]Equal contribution

[**]To whom correspondence should be addressed. E-mail: simpsonml1@ornl.gov or leor.weinberger@gladstone.ucsf.edu

This file includes:

Table of Contents

Introduction

The primary goal of this supplementary information document is to describe the mathematical and computational analyses used to analyze time-lapse fluorescence imaging of reporter gene expression that were used to generate noise maps and extract information on promoter dynamics and kinetics. We first describe the experimental methods used to create the lentiviral reporter vectors and the microscopy methods for obtaining single-cell trajectories for the construction of noise maps. We then summarize the analytical treatment of the two-state model of transcriptional bursting and describe the noise-map signature of transcriptional bursting.

EXPERIMENTAL METHODS

Cloning of lentiviral vector reporters

All reporter vectors are lentiviral vectors. DNA manipulations were performed using standard restriction enzyme cloning and PCR cloning techniques (1). All references to GFP here and in the main text refer to enhanced GFP, a.k.a. EGFP (Clontech Laboratories, Mountain View, CA) and encode a PEST destabilization domain (a.k.a d2EGFP). The LTR-d2GFP reporter vector (Ld2G) was cloned from the described LTR-GFP vector (2) by exchanging the EGFP coding region for d2EGFP obtained from pd2EGFP (Clontech Laboratories). The UBC reporter vector was constructed from the FUGW plasmid (3) by exchanging the GFP-WPRE coding region for d2EGFP. The EF1A reporter vector was constructed from the pLEIGW plasmid (4) by exchanging the IRES-GFP-WPRE coding region for d2EGFP. For the two-color assay, the d2EGFP within Ld2G was replaced by a mCherry cDNA to generate LmCh. Cloning

details are available upon request. All reporter vectors were packaged and concentrated as described (1).

Cell culture & time-lapse fluorescence imaging conditions

Jurkat T cells were maintained in RPMI medium 1640 with L-glutamine (Invitrogen, Carlsbad, CA), supplemented with 10% fetal calf serum and 1% penicillin-streptomycin. Cells were maintained at 37º C, 5% CO_2, under humidified conditions at densities of $2x10^5$-$2x10^6$ cells/ml. Cells were infected in culture medium at a multiplicity of infection (MOI) < 0.1 and flow cytometry analysis was used to assay MOI as described (2). In some cases, GFP-positive cells were enriched by FACS sorting to increase imaging throughput, but no difference in the noise maps could be detected between experiments on sorted and unsorted populations of cells (comparative data not shown). The EF-1αd2G + LTRmCh cell line is a two-color cell line where Jurkat T cells were first infected at an MOI < 0.1 with the EF-1α promoter driving d2GFP. For 2-color experiments, GFP-positive cells were FACS sorted, then infected with the LTR promoter driving mCherry at an MOI < 0.1, and FACS sorted again to isolate the newly mCherry-positive cells. This yielded a polyclonal population of cells with a single integration of EF-1α driving GFP and a single integration of the LTR driving mCherry within the same cell.

All time-lapse fluorescence microscopy was performed on live cells at 37ºC/5% CO_2 under humidified conditions. The following microscope setup was used: an Olympus DSU confocal microscope equipped with a WeatherStation environmental chamber (Precision Control Instruments), a Hamamatsu ORCA II ERG camera, a 40X UPLANSAPO oil-immersion objective (N.A. = 1.2), a metal-halide illumination/excitation source (Prior Lumen 200), a Prior automated linear-encoded X-Y stage, and Slidebook image acquisition software.

As described (5), live cells were immobilized on Matek™ glass bottom dishes and images were collected once every 10 min for 12 h: exposure times were set at 500 msec for all experiments and photobleaching of samples under these imaging parameters was not detected. Image processing to obtain cell trajectories was performed using established tracking and segmentation algorithms (5), the codes for which are available upon request.

After computer-automated collection of single cell GFP intensity trajectories each trajectory was manually "quality controlled" to remove outliers due to irregular cell morphology or movement during imaging. Up to 500-800 quality-controlled single cell intensity trajectories are collected per overnight experiment resulting in data collected from thousands of cells after a series of experiments.

TNF (or TNF-α) was obtained from Sigma Chemical Co. (St. Louis, MO), dissolved in DMSO, and added to cells at final concentration of 10ng/ml. For TNF addition experiments, cells were chronically exposed to TNF for 18hrs. In the wash experiments after the TNF 18 h incubation (SI Figure 17), the cells were then washed twice with PBS and plated for imaging as described above. Average time from wash to imaging was 1.5 h.

Cell Synchronization (see Fig. S2)

Jurkat T cells were synchronized using centrifugal elutriation as described (6). Flow rates were adjusted from 14.4 to 15.5 ml/min while kept at a constant spin of 2200g to collect the first fraction. For every 10-15-ml fraction collected, the subsequent fraction would be collected at a flow rate of 0.5 ml/min higher. To analyze synchronization, 1-mL samples were taken from each fraction, mixed with 1 mL of a 1% NP-40, 10 ug/mL propidium iodide (PI) solution (Sigma

Chemical) in PBS, and analyzed by flow cytometery. Approximately 1000 live cell counts were obtained per fraction and cytometer gates were drawn as described (6).

ANALYTICAL AND COMPUTATIONAL METHODS

Two-state model of transcriptional bursting

Transcriptional bursting is a model of gene expression where the expression rate is controlled by switching between discrete high and low transcriptional rates. The average rate is determined by the fractional amount of time spent in each of the two states. This model is consistent with transcription controlled through protein–DNA interactions at an operator site within the gene-promoter region or with the bursty expression of genes compacted in chromatin. To illustrate the model, we present equations adapted from an earlier analysis (7) with the simplifying assumptions that at the low expression state the transcription rate is 0, and that other than burst dynamics there is only one dominant time constant (usually either protein or mRNA decay dilution) represented by the rate constant γ_d. These assumptions are only made to lead to simple analytical expressions that aid in developing an intuitive understanding of the system, and are not meant to constrain the simulations provided below.

The 2-state model as described above. The gene transitions between active (G1; transcription rate =k_m) and inactive (G0; transcription rate =0) states. The fraction of time spent in state G1, O, is given by $O = \frac{k_{on}}{k_{on} + k_{off}}$.

The transcriptional bursting is represented by three model parameters (see Figure below): (1) the transcription rate in the high expression state, k_m, (2) the fraction of time spent in the high expression state, O, which we will also refer to as the 'on fraction', and (3) the kinetics of the switching between off and on

expression states, which is represented by k (referred to here as the burst kinetic rate), the sum of k_{ON} and k_{OFF}.

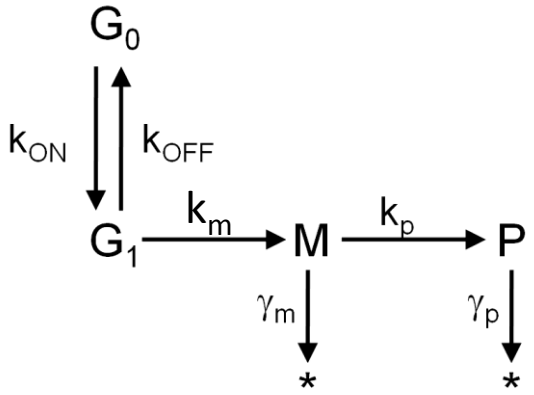

As reported (8), with these assumptions, the autocorrelation function of the noise, $\Phi(\tau)$, is

$$\Phi(\tau) \approx \frac{k_m Ob}{\gamma_d} be^{(-\gamma_d \tau)} + \left(\frac{k_m Ob}{\gamma_d}\right)^2 \frac{(1-O)}{Ok} \left(\frac{\gamma_d}{\left[1-\left(\frac{\gamma_d}{k}\right)^2\right]} e^{(-\gamma_d \tau)} + \frac{k}{\left[1-\left(\frac{k}{\gamma_d}\right)^2\right]} e^{-k\tau} \right), \qquad \text{(S-1)}$$

where b is the translational burst rate (average number of proteins translated from each mRNA). The average protein population, $\langle p \rangle$, is

$$\langle p \rangle = \frac{k_m Ob}{\gamma_d}$$

and the noise magnitude, CV^2 is

$$CV^2 = \frac{\Phi(0)}{\langle p \rangle^2} \approx \frac{b}{\langle p \rangle} + \frac{(1-O)}{Ok}\left(\frac{\gamma_d}{\left[1-\left(\frac{\gamma_d}{k}\right)^2\right]} + \frac{k}{\left[1-\left(\frac{k}{\gamma_d}\right)^2\right]} \right). \qquad \text{(S-2)}$$

The first term on the right, referred to as the shot-noise term (7), may be significant at (i) low protein population, (ii) values of O that approach unity (constitutive expression), or (iii) if $k >> \gamma_d$ (fast switching between expression states). Conversely, the second term on the right, referred to here as burst noise, is more prominent at (i) low on fraction, (ii) high protein population, or (iii) slow switching between transcriptional states ($\gamma_d >> k$).

The dominant-noise term—whether it is shot noise or burst noise—plays an important role in determining the noise structure. If the shot-noise term is dominant, CV^2 varies inversely with protein abundance, and correlation is determined primarily by γ_d. The shot-noise dominated noise map is indistinguishable from the constitutive expression noise map with most trajectories clustered around a diagonal line that runs through the origin (Fig. 2d, left graph, in the main text). Conversely, if burst noise is dominant, CV^2 is shifted upward and varies inversely with the on fraction and the switching kinetics. The correlation component of the noise also shifts inversely with the burst kinetic rate such that long on periods, followed by long off periods lead to large correlation values. The net effect of transcriptional bursting on the noise maps is a shift to the upper right quadrant as illustrated in Figures 1-2 of the main text.

Equation S-1 (above) shows how different gene-expression mechanisms differentially affect the noise structure. For example, translational bursting is represented by the parameter b, which modulates the magnitude of both shot and burst noise, yet has no effect on correlation as it does not appear in any of the exponential terms. Conversely, transcriptional bursting is

controlled by the parameters k_{on} and k_{off}, which in turn affect *O*, thereby increasing the magnitude of burst noise, and *k*, thereby increasing the burst-noise correlation time. As a result, transcriptional bursting has a noise signature that is distinct from that produced by translational bursting.

We define the noise ($N_i(t)$) of cell i as

$$N_i(t) \equiv \left(I_i(t) - g_i \cdot G(t)\right) \quad \text{(S-3)}$$

where $I_i(t)$ is the measured fluorescence intensity concentration of cell *i*, g_i is a gain factor for the amount of deterministic coupling of the general population trend into each individual cell *i*, and G(t) corrects for background fluorescence and any drift or general trend in fluorescence over time, and removes the average fluorescence level of each cell over the 12-hours of observation (9). This removal of the average level from each fluorescence trace effectively high-pass filters the noise (see Supplementary Information and (9)). Accordingly, we refer to the autocorrelation functions derived from the processed noise traces as high-frequency autocorrelation functions (HF-ACFs), and the noise maps with noise correlation and magnitude attributes presented in the current study are all HF noise maps.

Effect of LTR transcriptional stall on transcriptional bursting

To illustrate the effect of the LTR transcriptional stall burst behavior, here we model EF-1α and LTR promoters exhibiting the same base transcriptional bursting behavior that differ only in the transcriptional stall for the LTR promoter. This transcriptional stall is due to a nucleosome-with high affinity for a stretch of DNA at the nuc-1 position within the LTR that blocks RNAPII elongation, thereby delaying the start of the LTR transcriptional burst. We

model Ef-1α transcription with stochastic burst that, on average, are on for a duration of $\overline{\tau_{on}}$ followed by off periods of average duration of $\overline{\tau_{off}}$. We model the LTR transcriptional stall as a stochastic delay (average duration = $\overline{\tau_d}$) between the leading edge of the transcriptional burst and the actual start of LTR transcription (Figure below). To simplify the analysis, this model uses a lumped delay at the beginning of the transcriptional burst. Using this approximation,

$$O_{EF-1\alpha} = \frac{\overline{\tau_{on}}}{\overline{\tau_{on}} + \overline{\tau_{off}}}$$
$$O_{LTR} = \frac{\overline{\tau_{on}} - \overline{\tau_d}}{\overline{\tau_{on}} + \overline{\tau_{off}}} = O_{EF-1\alpha} - \frac{\overline{\tau_d}}{\overline{\tau_{on}} + \overline{\tau_{off}}}, \quad \text{(S-4)}$$

and the major effect of the transcriptional stall is seen as a reduction in the measured *O* for LTR compared to Ef-1α.

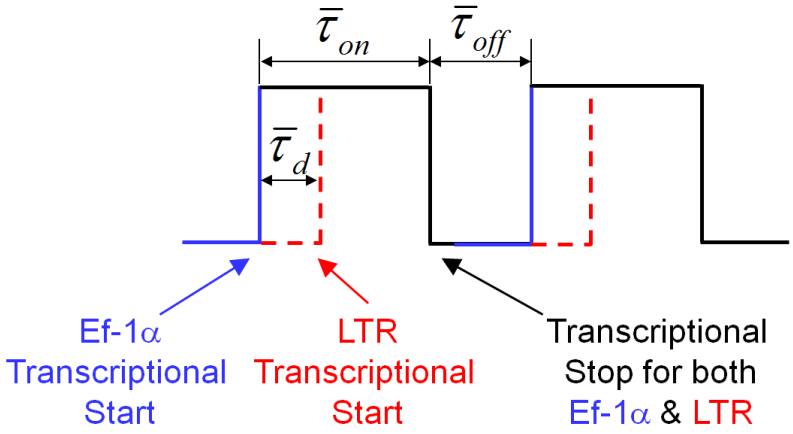

Although the period (τ_{on}+ τ_{off}) remains constant, the transcriptional stall may affect the measured transcriptional burst dynamics by changing the value of *k*. Using the model above

$$k_{on} = \frac{1}{\overline{\tau_{off}}}$$

$$k_{off} = \frac{1}{\overline{\tau_{on}}}$$

$$k_{on\_s} = \frac{1}{\overline{\tau_{off}} + \overline{\tau_d}}$$

$$k_{off\_s} = \frac{1}{\overline{\tau_{on}} - \overline{\tau_d}},$$

where the *s* subscript indicates the effective values for k_{on} and k_{off} including the transcriptional stall. For this case,

$$K_s = k_{on_s} + k_{off_s} = \frac{\overline{\tau_{off}} + \overline{\tau_{on}}}{(\overline{\tau_{on}} - \overline{\tau_d})(\overline{\tau_{off}} + \overline{\tau_d})}, \qquad \text{(S-5)}$$

and if $\overline{\tau_d}$ is small compared to $\overline{\tau_{on}}$ and $\overline{\tau_{off}}$

$$K_s \approx K.$$

The measured noise maps show that LTR has a higher CV^2 (which is indicative of a lower on fraction), but has a nearly identical distribution of HF-$\tau_{1/2}$ (see figure S-4). This would seem to indicate that for most integration sites, $\overline{\tau_d}$ is small compared to $\overline{\tau_{on}}$ and $\overline{\tau_{off}}$ and that the major effect of the transcriptional stall is an increase in the noise magnitude. However, this general observation should not be applied to specific cases. In some integration sites, $\overline{\tau_d}$ might significantly alter the bursting dynamics.

High-frequency noise processing focuses on intrinsic noise

Other than resolving the ambiguity between low frequency gene expression fluctuations and differences in basal gene expression levels (SI Figure 1), the individual cell noise mean suppression and high-pass filtering essentially focuses on high frequency intrinsic noise and de-focuses the low-frequency extrinsic noise (SI Figure 2). Analogous to gating in flow cytometry (to reduce extrinsic noise sources related to cellular state and cell cycle), this *in silico* high-pass filtering reduces low-frequency extrinsic noise from all extrinsic noise sources. To observe this effect, we simulated constitutive gene expression using various levels of extrinsic noise using the intrinsic and extrinsic noise-simulation model described in the Supplementary Information and reference (10). Since the intrinsic noise is directly modulated by gene circuit structure and function, the high-pass filtering enhances the quality of autocorrelation analysis to understand the function of gene circuits without any additional extrinsic noise background. Finally, it is worth noting that although infinite duration analysis and measurements would be informative, experimental limitations occlude this possibility. Therefore, it is precisely the short-duration expression windows we are analyzing that the individual cell 'sees', and phenotypic dynamics and decisions take place over these expression windows. So although, at first, the multiple-step noise-processing algorithm from (9) was developed to resolve various experimental obstacles, in the end, it provides an *in silico* tool with a biological view that is highly relevant *in vivo*.

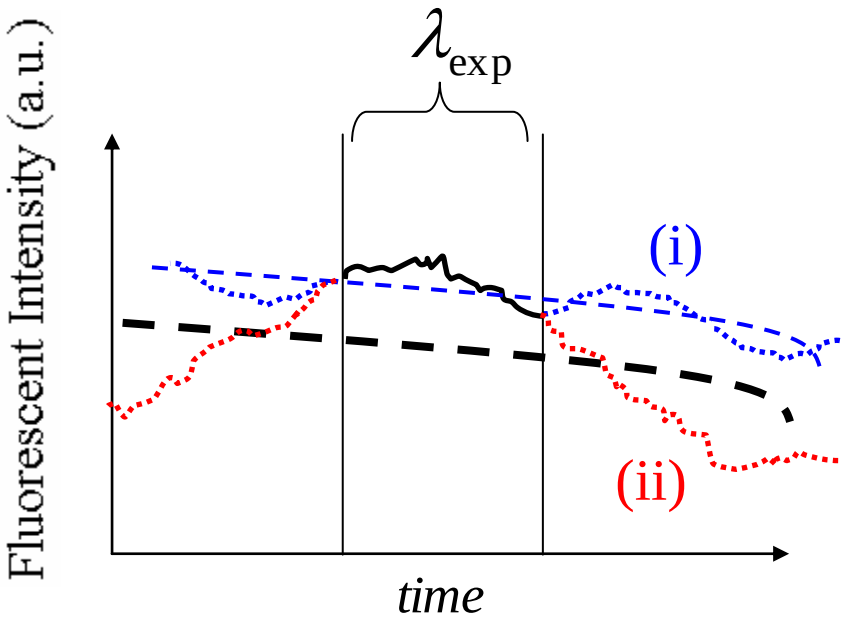

SI Figure 1: Baseline expression shifts are indistinguishable from low-frequency fluctuations. Distinguishing between baseline expression level shifts and long correlation fluctuations in a limited imaging duration window becomes very difficult. A single-cell expression level is measured over an experimental imaging window λ_{exp} (solid black) and is found to exist above the deterministic population trend (A(t)), (thick dashed black). It is difficult to determine if the signal (dotted blue, (**i**)) is fluctuating quickly about a possible baseline shift of the deterministic trend (thin dashed blue), or is a segment sampling of a low frequency fluctuation (dotted red, (**ii**)) fluctuating about the true deterministic trend (thick dashed black). Both possible fluctuations (i and ii) may be legitimate samplings of the correlation spectrum for a given gene circuit.

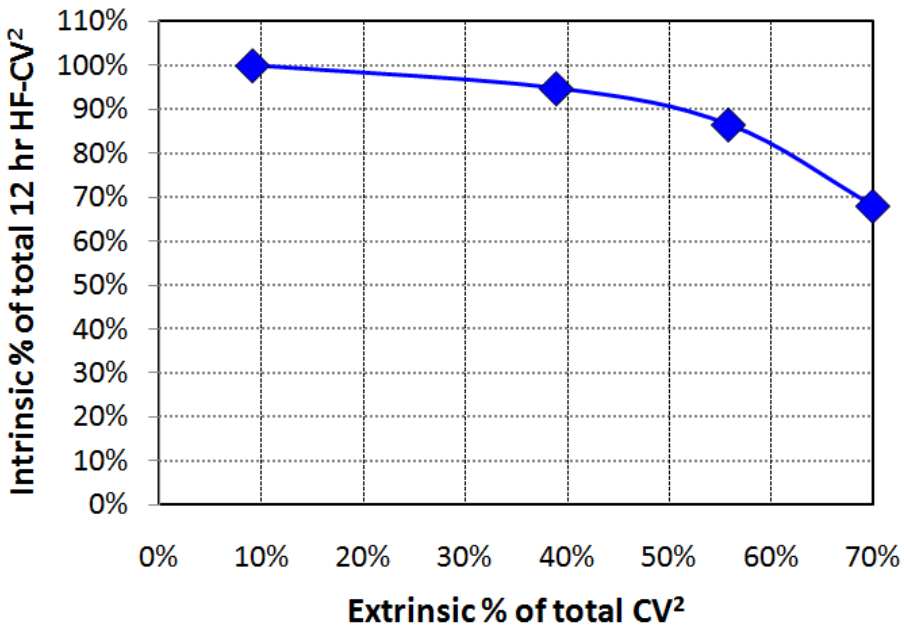

SI Figure 2: HF-processing focuses on intrinsic noise and filters out extrinsic noise. Using the described intrinsic/extrinsic noise simulation, we can estimate how much noise magnitude is filtered out or emphasized with the 12-hHF-noise processing. For a large range of extrinsic noise contribution, intrinsic noise contribution is enhanced ~1.1-2.3 times of the total noise, while extrinsic noise is de-emphasized (filtered) down (e.g. 55% extrinsic of total noise filters down to ~15% of total noise, 40% of total to 5% of total, and so on).

Noise Mapping

Each point on the noise map represents the noise magnitude and correlation of an individual cell relative to what we have termed the noise "bias vector". That is, the noise-map location (which we designate as the noise vector $\vec{N}$) of the individual cell *i* is given by

$$\overrightarrow{N_i} = \log_{10}\frac{\tau_{i1/2}}{\tau_{bias1/2}}\hat{t} + \log_{10}\frac{CV_i^2}{CV_{bias}^2\left(\langle fl_i \rangle\right)}\hat{c} \qquad \text{(S-6)}$$

where $\hat{t}$ and $\hat{c}$ are unit vectors in the *x* and *y* directions on the noise map; CV_i^2 and $\tau_{i1/2}$ are the measured high-frequency CV^2 and half-correlation time of cell *i* (see discussion above about high-frequency processing); $CV_{bias}^2\left(\langle fl_i \rangle\right)$ and $\tau_{bias1/2}$ are the components of the bias vector; and $\langle fl_i \rangle$ is the average fluorescence measured from cell *i*. In the ideal case, the bias vector would represent the noise of true constitutive expression whose CV^2 would depend on the GFP concentration (i.e., fluorescence level), while the half-correlation time would be constant for any GFP concentration.

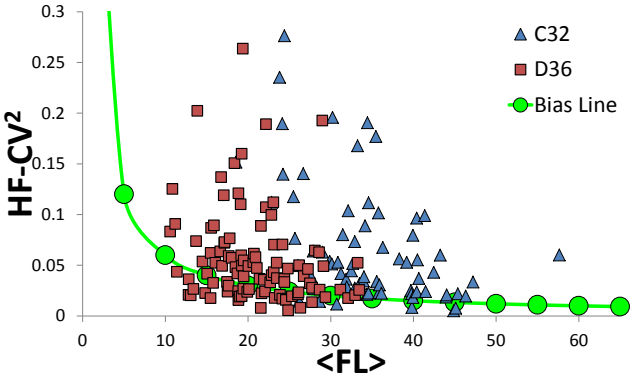

SI Figure 3: Least bursty isoclones to determine the bias vector. HF-CV^2 vs. average fluorescence level for clones C32 (58 cells) and D36 (87 cells). From these measurements the CV^2 component of the bias vector (green line) was found as 0.6/<*fl*>.

We used both experimental and simulation approaches to determine the bias vector for the 18-h experiments presented in the main text. The same bias line is applied to 12-h experiments after adjusting for experiment duration with simulations (Figure S1). Experimentally, we examined the half-correlation times measured for isooclonal populations carrying the Ld2G circuit in search of integration site(s) where transcriptional bursting was having the least pronounced affect on noise behavior (i.e. low half-correlation times). Starting with a library of clones (2, 11), we identified two clones with low half-correlation times compared to other isoclonal populations and the polyclonal measurements. Moreover, in addition to correlation times these isoclones displayed considerably lower noise magnitude compared to other clones (Figure S1).

Accordingly, we based our 18-hr bias vector on these two clones, SI Figures 3 and 4, which gives

$$CV^2_{bias}\left(\langle fl \rangle\right) = \frac{0.6}{\langle fl \rangle}$$

$$\tau_{bias\_1/2} = 1.92 hours \qquad \text{(S-7)}$$

The high frequency $\tau_{1/2}$ of these clones exhibits distributions with one mode peaking between 1.5 and 2.0 h, and additional secondary peaks between 2.25 and 4 h (SI Figure 4). The higher correlation peaks are evidence of transcriptional bursting in these clones, but the strong lower mode indicates that transcriptional bursting is not as pronounced in these clones as it is in others.

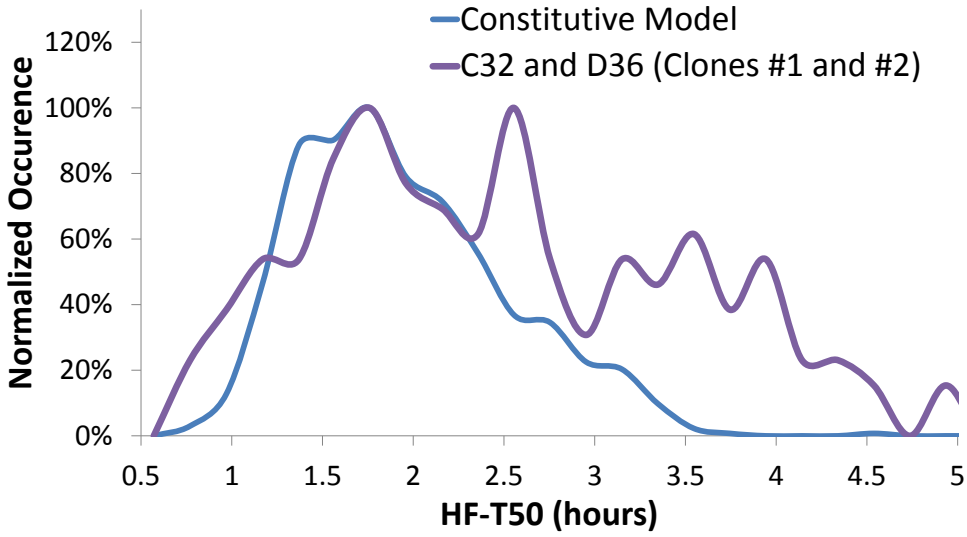

SI Figure 4: Isoclones with lowest correlation time to determine correlation bias vector. The distribution of HF-T50s measured for clone C32 and D36 (purple). The bias vector value of HF-T50 was selected as 1.92 hours. The blue line shows the simulated HF-T50 distribution for constitutive expression (see Table S-1 below) and HF-T50 = 1.92 h, which is seen to fit well with the lower mode of the C32 and D36 HF-T50 distribution. The higher HF-T50 peaks in the isoclone distribution (purple) are indicative of some transcriptional bursting in these clones.

To simulate the least bursty clones, the GFP half-life was set to a measured 2.5 h in agreement with its reported value (12, 13), and the mRNA half-life was selected to have the largest possible value consistent with the kinetics of GFP fluorescence approaching steady-state after activation with TNF and with the shortest measured $\tau_{1/2}$ (LTR +TNF) (SI Figures 5 and 6). The HIV LTR encodes multiple NFκB sites and is potently activated by TNF across all integration sites (14). Consistent with the model that enhancers increase the probability of transcriptional initiation (15), exposure to TNF results in faster kinetics for the LTR.

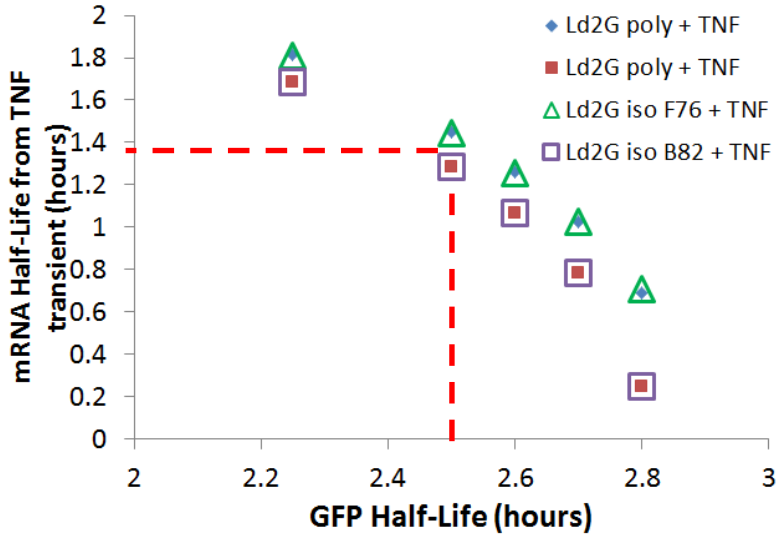

SI Figure 5: An mRNA half-life of ~100 min was estimated using transient times with TNF induction of two different LTRd2GFP polyclonal and two different LTRd2GFP isoclone experiments.

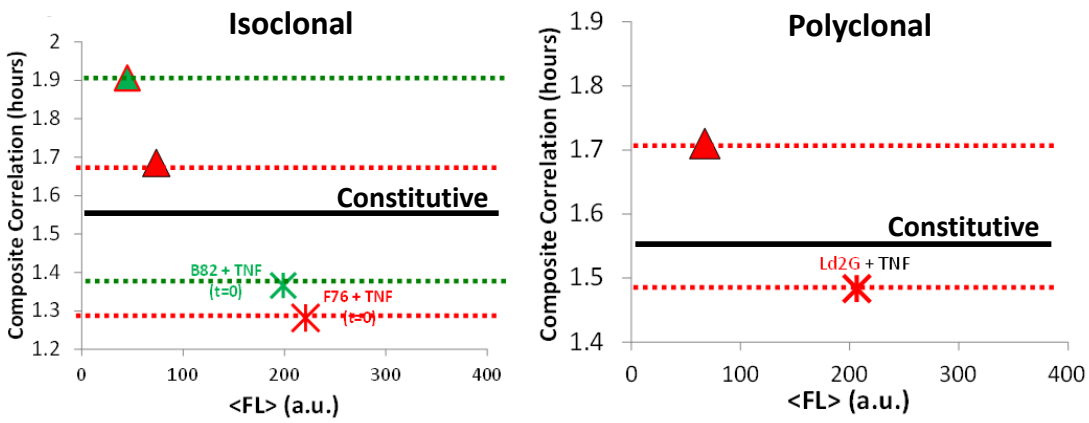

SI Figure 6: Second approach to mRNA half-life estimation using the maximal decrease in correlation time via TNF induction using polyclonal and isoclone experiments. Constitutive line is based on simulation of Table S-1 and an mRNA half life of 100 min. Similar to Figure 5 in the main text, here the non-continuous induction with TNF falls below the simulated constitutive line. These are based on least bursty isoclones which may have been additionally bursty causing this shift, in which case the constitutive bias line used would minimize the observed system-wide burstiness, or the non-continuous modulation with TNF may also strongly affect correlations.

The mRNA half-life was estimated using the correlation times (SI Figure 4), the transient expression time constants from TNF–induced conditions in LTR isoclones and polyclones (SI Figure 5), and the magnitude of correlation shift with TNF addition (SI Figure 6) under the assumption that TNF addition cannot speed up the kinetics faster than the underlying primary time constants. The three approaches are consistent with one another and used for the following simulations in the main text (Bias line and Figure 3B).

Parameters for the model are given in Table S-1 below. This model was used to generate the non-bursty noise map origin in Figure S1 and 3B.

Table S-1. Parameters used in simulations and experimentally determined burst dynamics

Parameter	Value used or quantified	Range from literature	Resource
<GFP>	30000 – 120000		Singh et al., *BoJ* (2010)(16)
b **(GFP/mRNA lifetime)**	420 Or 115 mRNA/h	662 (max value) 180 mRNA/h (max)	Schwanhäusser et al., *Nature* (2011) (17)
mRNA H-L	100 min	Lands within possible values, on lower end	Sharova et al., *DNA Res* (2009) (18)
GFP H-L	2.55 h	Measured with cycloheximyde addition	Data not shown.
Burst Frequency	0.003-0.01 min^{-1} (0.01-0.057 min^{-1} for EF1A and UBC promoters, Figure S7)	0.02-0.055 min^{-1}	Suter et al., *Science* (2011) (19)
Burst Size	100 – 300 (# of mRNA)	Average = 40, max = ~200 (w/TetO promoter)	Raj et al., *PLoS Biology* (2006) (20)

CONTROL: Testing for lentiviral integration hotspots

To control for potential bias introduced by possible oversampling of lentiviral integration "hotspots" (21), we analyzed random sub-clusters of 500 cells each in the Ld2G poly dataset. If the data were dominated by integration hotspots, the hotspots would be statistically underrepresented in a proportion of sub-clusters, and the sub-clusters would exhibit different noise-map centroid positions. However, we obtained a tight clustering of noise-map centroid positions for all sub-clusters (SI Fig. 7), providing strong evidence against oversampling of lentiviral integration hotspots.

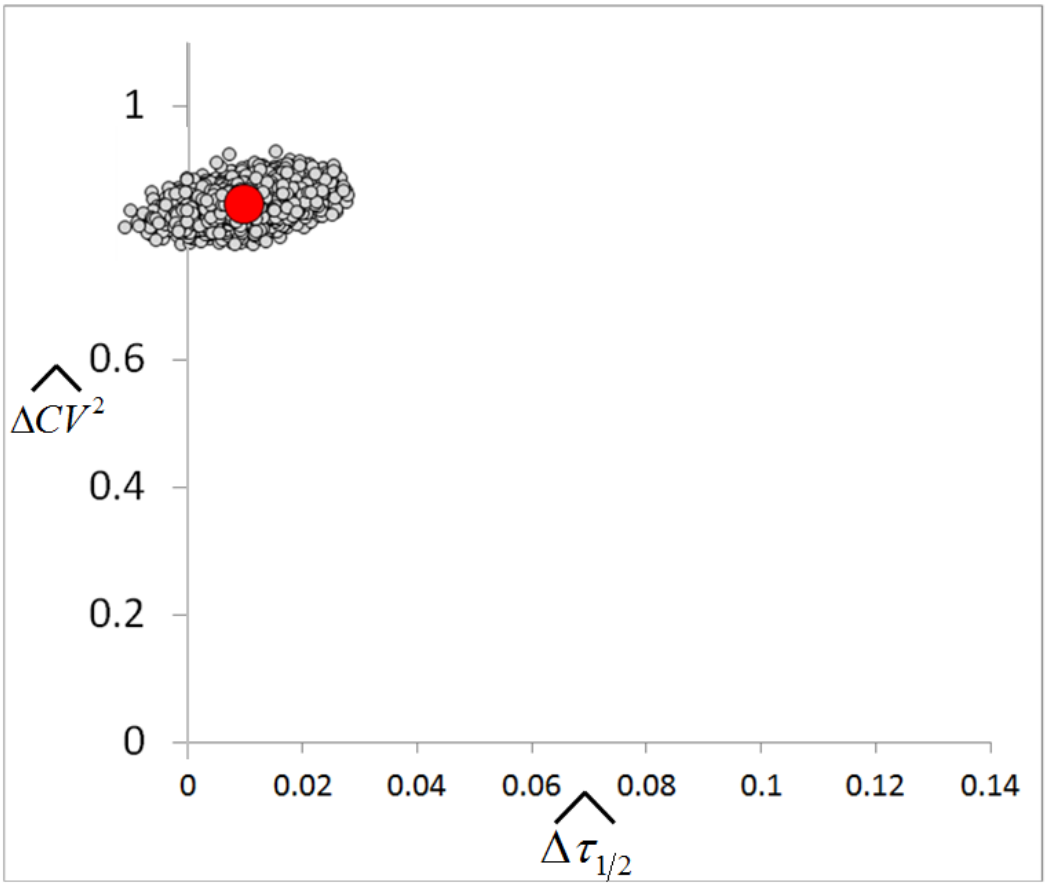

SI Figure 7: Control for potential bias introduced by possible oversampling of lentiviral integration 'hotspots'. Each of the gray points above represents the noise-map centroid of one sub-cluster of 500 cells randomly sampled from the entire population of cells. These random sub-clusters are closely distributed around the noise map centroid of all the cells (shown in red). If the data were dominated by integration 'hotspots', these hotspots would have been statistically underrepresented in a proportion of sub-clusters, which would have been reflected in different noise-map centroid positions.

Effect of longer sample recovery

An additional 6 h of sample recovery before imaging had no affect on the resulting composite noise-map coordinate. The coordinates for a combination of isoclonal experiments, and the composite coordinates for over 1000 cells of the Ld2G polyclonal experiment is shown in SI Figure 8.

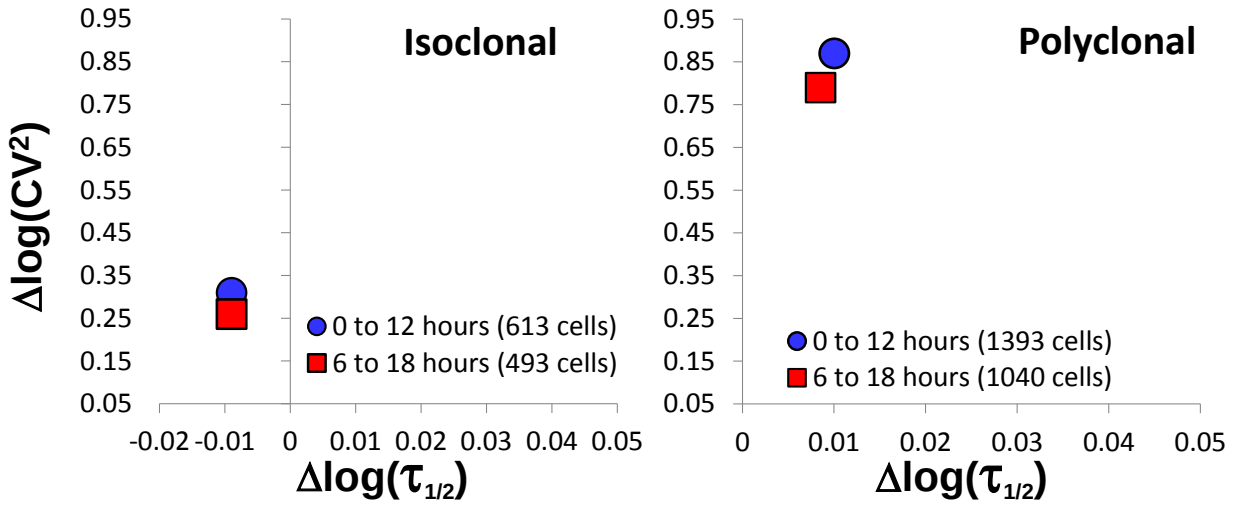

SI Figure 8: Six additional hours of sample recovery do not influence noise map coordinates. This was performed for both a combination of LTR d2GFP isoclones (left) and the polyclonal population (right).

Cell-cycle synchronization

Cell synchronization was performed using centrifugal elutriation (see Cell Synchronization section) yielding a synchronized population containing ~85-90% of cells in the G1 phase of cell cycle. To obtain sufficient cell counts, three elutriated fractions were pooled together; each fraction comprising the pool contained cells synchronized at 92.6% (yellow), 83.9% (green), and 86.4% (blue) in G1 phase (shown below as percent max versus FL2 area). The control population contained a population synchronized in G1 to about 68% (red).

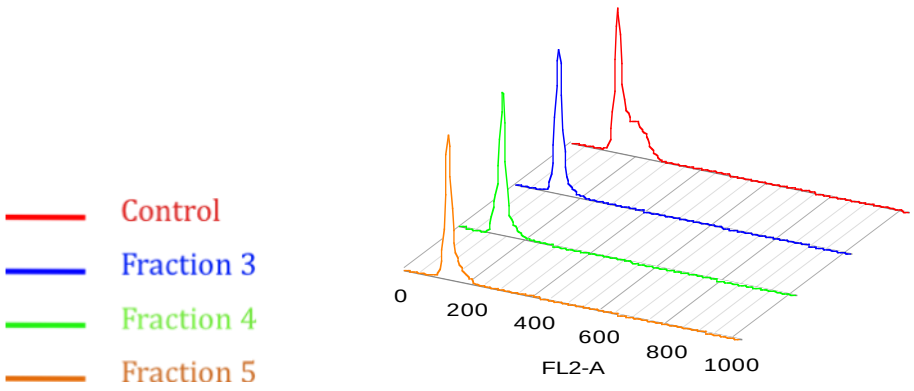

SI Figure 9: Distributions of cellular elutration for isolating cells in G1 phase.

The pooled fractions (85%-90% synchronized in G1) were imaged (using the same imaging parameters as described above) to obtain noise maps. The noise maps for a G1-synchronized Ld2G population were then compared to the noise maps of an unsynchronized Ld2G population to calculate noise-map centroids, in order to check for any differences between synchronized and unsynchronized cells (Figure S3). No significant difference could be found between synchronized and unsynchronized Ld2G cells as evidenced by the centroid locations in the noise map space (Figure S3).

To further determine if there are differences between synchronized and unsynchronized cell populations, we compared the HF-T50 distributions. Both synchronized and unsynchronized cells were shifted more in HF-T50 than the constitutive model (SI Figure 10) with the mean of the shift being the same for both synchronized and unsynchronized Ld2G populations.

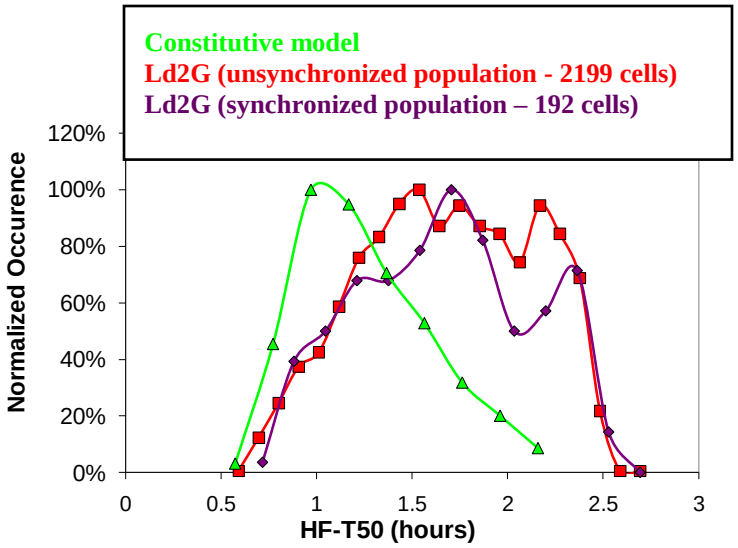

SI Figure 10: HF-T50 distribution comparison of synchronized versus unsynchronized populations. Comparison of HF-T50 distributions for the constituitive model (green), an unsynchronized Ld2G cell population (red) and a synchronized Ld2G cell population (purple). The constitutive distribution is the measured 'most constitutive' distribution described above for clones C32 and D36. No significant difference could be detected between the the means or medians of the Ld2G synchronized versus unsynchronized populations; peaks in the synchronized Ld2G cell population have smaller cell numbers than the unsynchronized population.

Finally, we compared the first 6 and last 6 h of synchronized Ld2G population imaging to test if the transcriptional burst frequency was changing during cell-cycle progression. The results show that the Normalized Composite Autocorrelation (NCAC)(5) during 0-6 h yields a slightly shorter (but not statistically significant) HF-$\tau_{1/2}$ compared to 6-12 h.

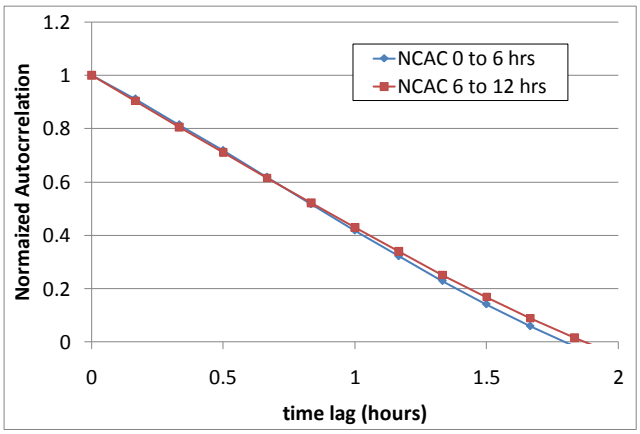

SI Figure 11: Comparison of cell-cycle dependent autocorrelation in a synchronized population.

Distinguishing behavioral noise shifts with limited duration experiments

A significant universal drawback of time-lapse microscopy is the limited time that one has in which to conduct experiments. This is usually due to sample stability, the biological process itself being difficult to observe for long time periods, or simply the inability of the researcher to run truly "infinite duration" experiments. The limited-duration fluorescence signal causes variability in the measurement that must be quantified to distinguish between differences in measurement and differences in the underlying biological behavior.

The following two sections are used to estimate error bars for population centroids in the noise map and the modulation in single-cell scatter as a function of number of cells collected and experiment duration. Scatter decreases with increasing cells in the ensemble and observation duration. Centroids of both isoclone (SI Figure 12) and polyclone populations (Figure S4) separate from one another and are statistically significant even though their single cell scatters may be large or have significant overlap in the main text figures.

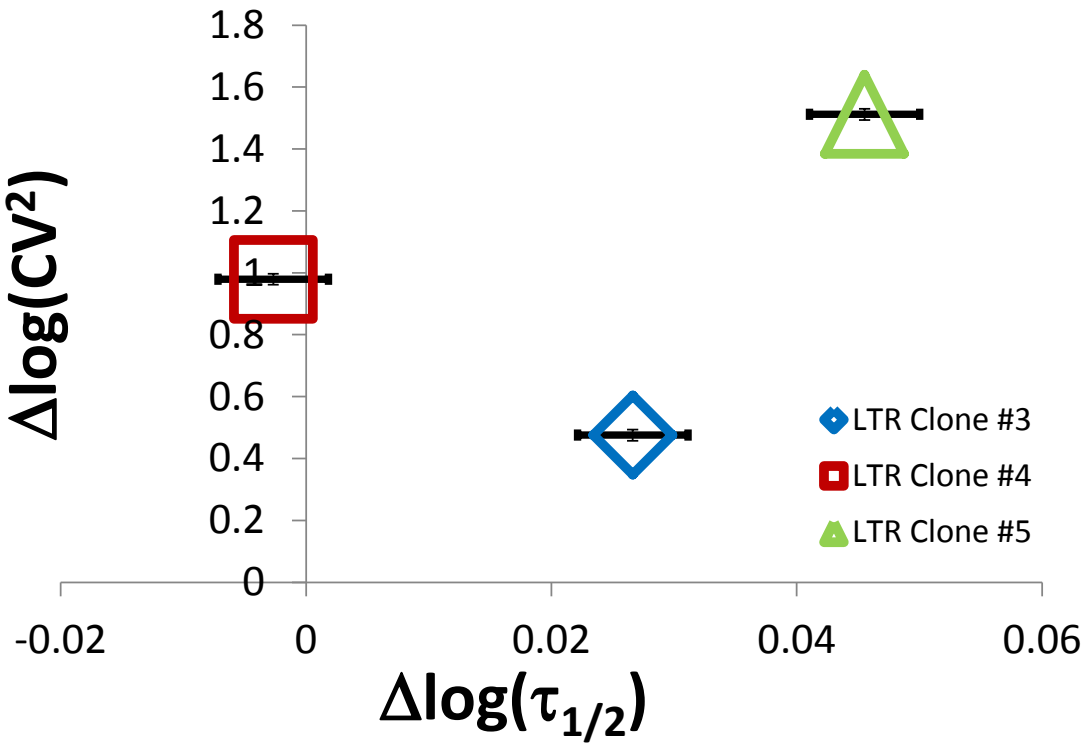

SI Figure 12: Centroid representation for three isoclones. Centroids for LTR isoclones from Figure 2 in the main text. Error bars for both axes are small and appear inside each data point symbol.

Noise-map centroid error-bar estimation

Centroid error bars were estimated by sampling 10,000 subgroup ensembles of various sizes from the experimental single-cell Ld2G polyclonal scatter that has ~2.5k cells. 10-k centroids were calculated from the 10-k subgroups of each ensemble size, and +/- 1 σ error was calculated and plotted for each noise-map axis for Supplementary Figure S4.

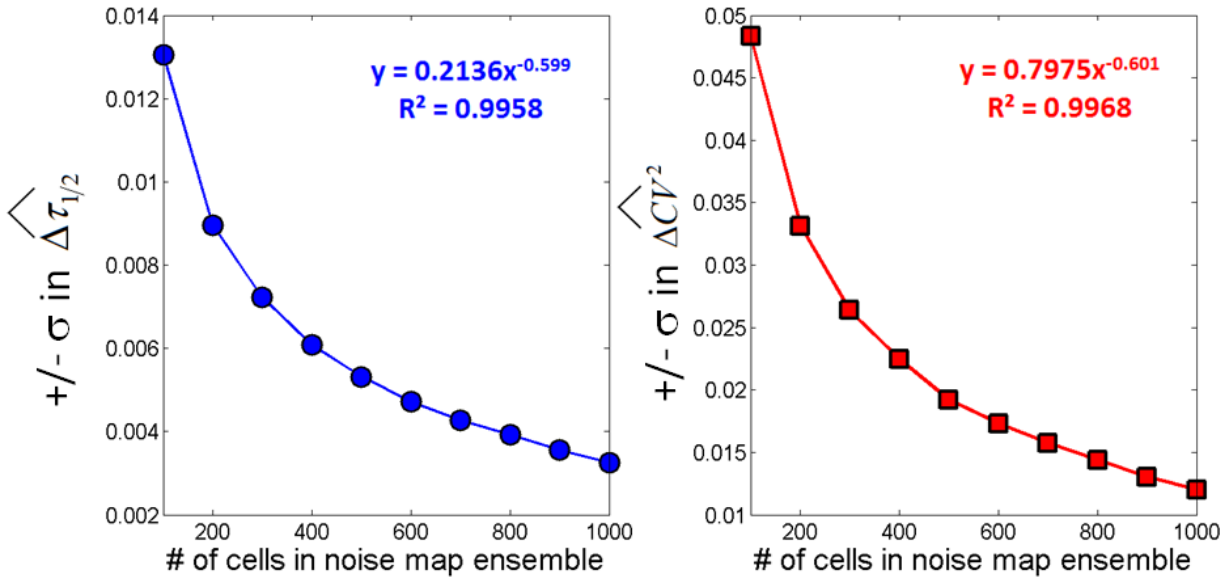

SI Figure 13: Noise variability dependence on number of cells in experimental ensemble. Centroid error bars for normalized $\Delta\tau_{1/2}$ (left) and normalized ΔCV^2 (right) estimated for the largest experimental polyclonal noise map (Ld2G) with ~2500 individual cell trajectories. Error shown for sampling of 10,000 subgroup ensembles as the number of cells in the ensemble is varied (x-axis).

Dependence of noise map variance on experiment duration

In the polyclonal noise-maps (Figures 3B and Supplementary Figure S1), the variance or "spread" in data points (i.e., cell trajectories) used to create each noise map is partly due to these differences in burst kinetics arising from the sampling of many integration sites (Fig. 3B), partly to the inherent limited-duration nature of imaging experiments (See SI Figures 14 and 15 below), and partly to the inherent cell-to-cell variation or limited time-duration imaging of each individual cell. Strikingly, the degree of spread in the isoclonal noise maps (Figures 2D) is similar to the spread observed for the polyclonal LTR noise map (Figure 3B), arguing that cell-to-cell variation, in addition to integration-site differences, must account for a large degree of the polyclonal scatter. Notably, the LTR polyclonal noise map still has a larger spread than any one of the individual isoclone noise maps alone.

Since all of the noise maps are based upon limited data from finite-duration imaging experiments, we tested how the duration of the experiment contributes to the cell-to-cell variance observed in noise maps (See SI Figures 14 and 15 below). Simulation of constitutive gene expression and imaging results show that experiment duration clearly puts a boundary on the length of correlation time than can be resolved, with longer experiments allowing longer correlation times to be resolved (SI Figure 14, panel a). In addition, simulations of constitutive expression show a marked contraction of the spread in data points for longer duration experiments (SI Figure 14, panel b). This contraction occurs because at the infinite duration limit the noise map collapses into a single point at the origin (8). In addition, panel b demonstrates how the high-frequency noise magnitude and correlation (see (9, 10) for review) compare to the true or infinite-duration noise-attribute values as a function of experiment duration. Using this calculation, we observe that constitutive experiments of 12-h duration, such as those presented

here and in a previous study (9), represent up to ~60% of the true underlying stochastic process. For experiments of durations greater than 60 h (or 2.5 days), the composite noise of high frequency (HF)-sampled experiments approaches true or infinite duration behavior. Of note that for 2-state bursty simulations, covering a range of parameter space, 12-h experiments represent about a third of noise magnitude and correlation of true infinite duration values (data not shown). The experimental data show similar trends with the correlation time boundary being extended along with a rotation and narrowing of the noise-magnitude axis spread in longer imaging experiments (SI Figure 14, panel c). SI Figure 15 further explores the trend by quantifying spread, centroid coordinate, and variability for an experiment analyzed from 6 to 24 h of data.

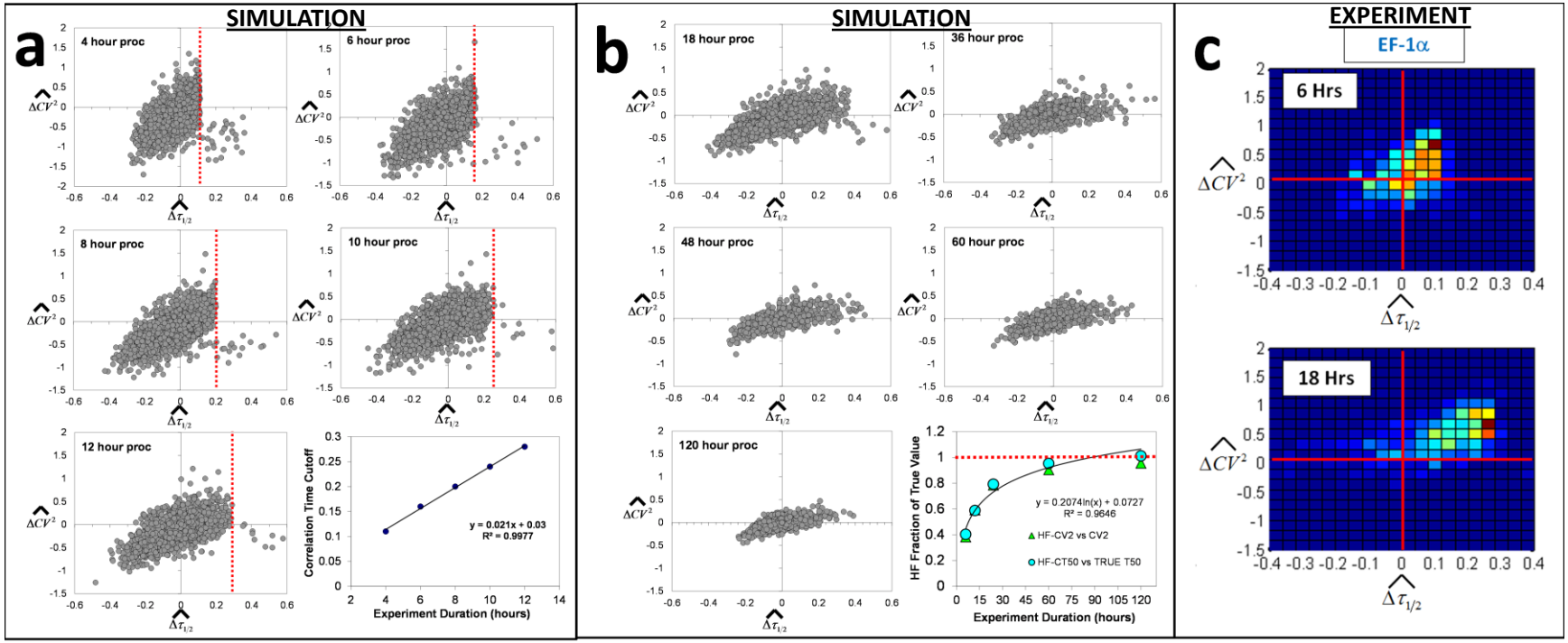

SI Figure 14: The variance (or spread) of a noise map is due to both the limited-duration of imaging experiments and intrinsic cell-to-cell variation. (a). Noise map signatures of constitutive expression simulations for 4- to 12-h durations. The graph shows a linear increase in the noise-map-correlation time cutoff with increasing experimental duration. (b) Simulated noise-map signatures for durations of 18–120 h. As simulation-experiment duration increases, the composite high-frequency noise magnitude and correlation (9, 10) approach their true, infinite-duration values. (c) Experimental, polyclonal noise-probability density maps of the Ef1α promoter data for 6- and 18-h durations. Similar to the simulation cases in panels *a* and *b*, the increased duration signature has an extended correlation cutoff, slight rotation, and decreased noise-magnitude spread.

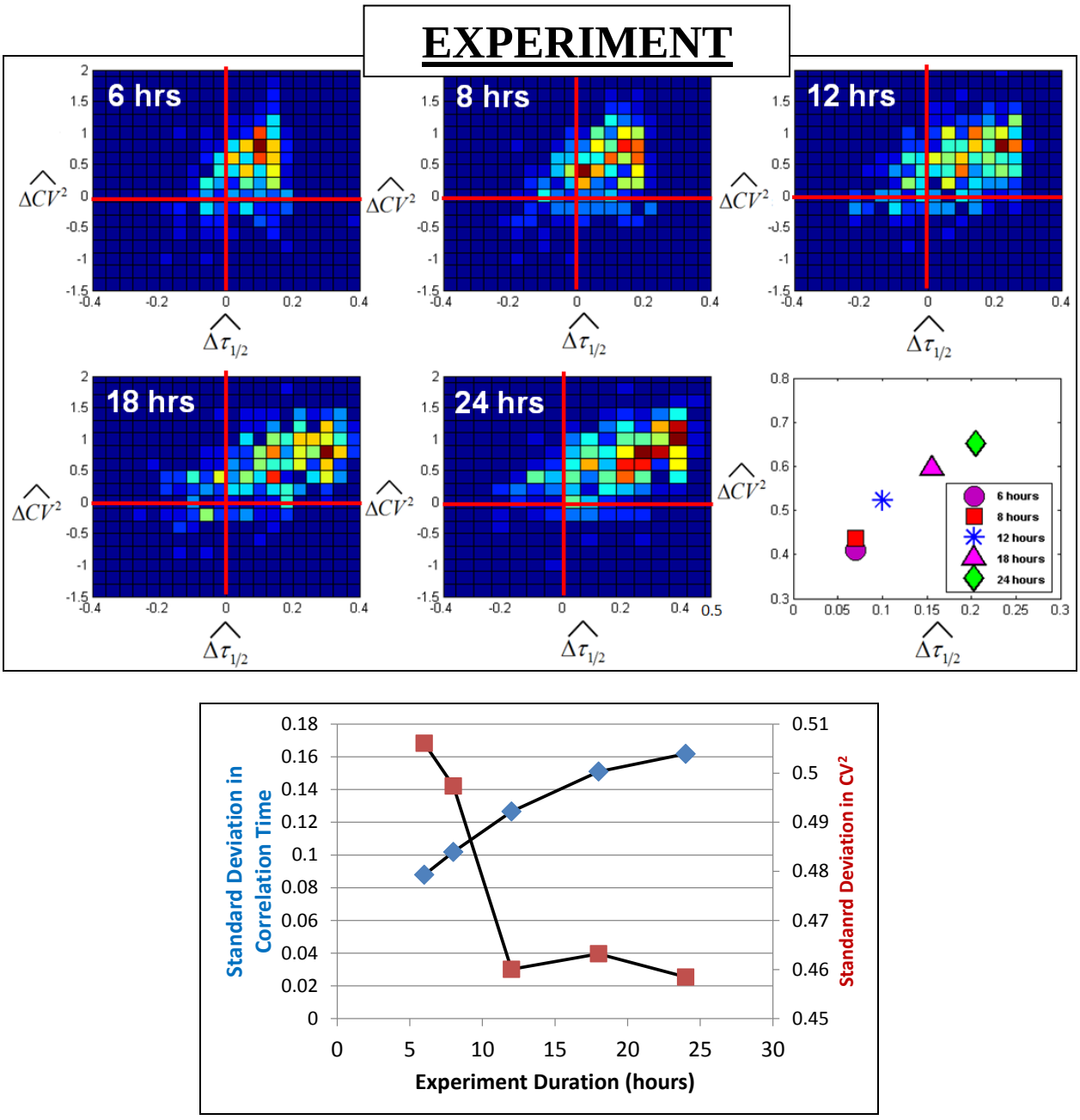

SI Figure 15: **Noise-map rotation, narrowing, and shift with increasing experiment duration.** (**Above**) A polyclonal experiment is processed for durations ranging from 6-24 h. The correlation-time cutoff gets extended in parallel to a rotation and shift to the upper-right-hand quandrant. Centroids of each noise-probability density map are also plotted to the lower right. (**Below**) The standard deviation of the single-cell noise-map spread decreases in the noise magnitude axis and increases in the correlation axis.

Are noise map shifts due to extrinsic noise?

In addition to transcriptional bursting, extrinsic noise (22) could be responsible for the measured noise-map shifts to the upper right quadrant. However, a principal advantage of high-frequency (HF) processing is that it focuses on high-frequency intrinsic noise, which is directly modulated by gene circuit structure and function while de-emphasizing lower-frequency extrinsic noise. To examine extrinsic noise-mediated shifts in HF noise maps, we simulated constitutive gene expression with various levels of extrinsic noise in the noise-simulation model described in the Supplementary Information of Austin *et al*., (10). The figure below shows the unfiltered and HF-mediated shifts in the average noise-map locations for extrinsic noise levels of 9, 39, and 56% of total noise. Although the unfiltered noise-map locations show considerable movement away from the origin with the addition of extrinsic noise, the HF-processed points remain contained in a region near the origin. As a result, the noise-map shifts shown in the main text cannot be accounted for by assuming large amounts of extrinsic noise.

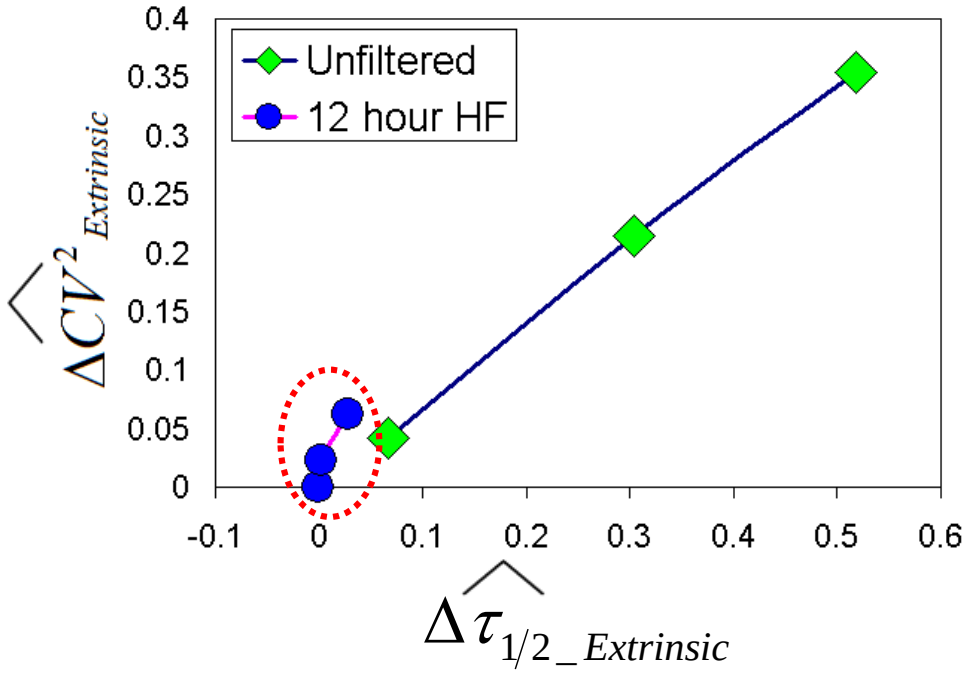

SI Figure 16: 12-hour HF-noise filtering of extrinsic noise.

Sub-cluster processing of polyclonal experiments for "effective isoclones"

To quantify the intensity-dependent transcriptional burst dynamics a sub-cluster processing approach of the polyclonal population was applied to the collected intensity trajectories. The total number of intensity-dependent sub-clusters was selected to minimize variability due to finite-duration experiments and cell-to-cell. GFP intensity trajectories were sorted into clusters based their individual final intensity concentration (Supplementary Figure S6). Here it is assumed that each sub-cluster represents an "effective clone" for a given intensity range. A previously reported noise-processing algorithm was applied separately to each sub-cluster (9), and composite noise magnitude defined by the cluster composite coefficient of variation (σ from composite autocorrelation function divided by the cluster mean intensity), and average intensity concentrations were extracted. The resulting LTRd2GFP (Ld2G) polyclonal noise trend including ~2000 cells is represented in Figures 4B-C. A single burst model line (Methods) describes most of the sub-cluster noise magnitude trend (Figure 4C). Sub-clusters at higher abundances appear to deviate to higher noise magnitudes. Equivalence of the sub-clustered processing to isoclones is seen with conventional flow cytometry measurement of isoclones in Figure S6. Similar equivalence is observed with exogenous drug addition (Figures 5B and S6).

Sub-cluster processing of isoclones fall along different regions of the sub-clustered polyclonal trend

To examine the degree to which the polyclonal sub-clustered noise and burst trends truly represent a large range of isoclone behavior, we processed individual isoclones in an identical manner. If the polyclonal trend represents a range of isoclones then the isoclone trends would land along the polyclonal trend, according to their respective abundance range. This is observed in SI Figure 17. Note that isoclonal population F76 curls between the low and high abundance domain pivot of the noise signature, while isoclonal population F32 lands on the upward high abundance and CV trend. This control demonstrates that among the isoclones sub-clustered, a single isoclone cannot describe the full polyclonal behavior quantified. An isoclone with its TNF addition counterpart and shift are plotted to the right.

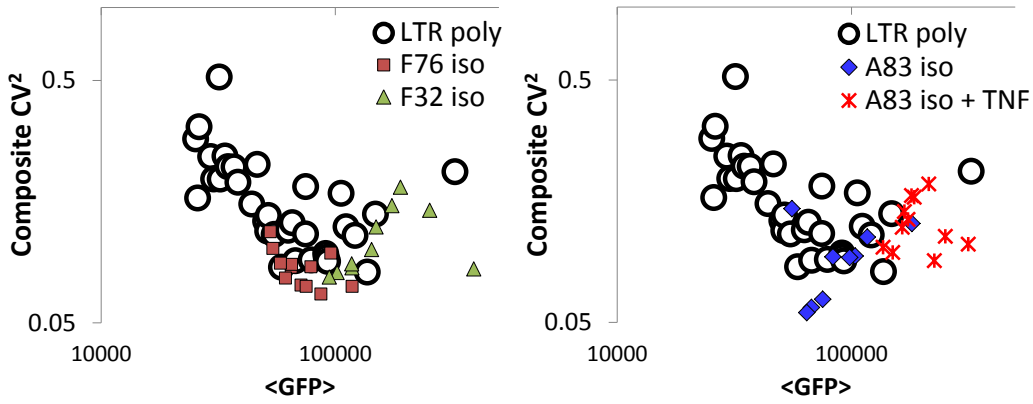

SI Figure 17: Sub-cluster processing of LTR isoclones. Four isoclone populations were processed by sub-clustering by expression levels (left), two of which are before and after TNF addition (right). The results demonstrate that the noise of individual clones contribute to specific regions of the global polyclonal signature (empty circles).

Recovery of noise map centroid after addition and wash of TNF

To further validate that a direct modulation of transcription is occurring with the addition of TNFα to the LTR promoter, a TNFα wash control was performed to observe a relaxation of noise map centroid back to the untreated state.

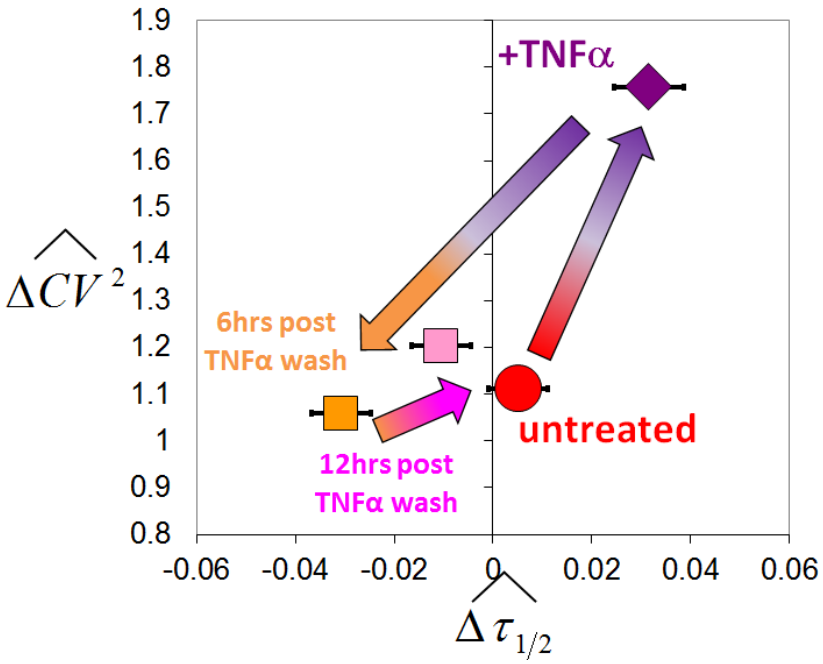

SI Figure 18: Sub-cluster processing of LTR TNF poly and LTR TNF WASH poly. With washing TNF the noise map centroid gradually returns to the approximate position of the untreated Ld2G poly centroid. Initially the TNF increases noise magnitude as the TNF sub-clusters fall on the high abundance, high burst size and magnitude parts of the non-TNF trends.

Noise and burst analysis of Ld2G poly exposed to exogenous trichostatin A (TSA)

In addition to TNFα, we treated the polyclonal population with trichostatin A (TSA), a histone deacetylase inhibitor, and observed an increase of all clones to higher abundances, an increase in BS, and a roughly constant BF (SI Figure 19). Collectively, the TNFα and TSA burst trends following the non-drug trends, and switching burst dynamic regimes at the same abundance threshold, suggests that both promoter regulatory sequence and local chromatin structure contribute and shape a burst dynamic landscape. The integration site landscape synergized with a promoter sequence provides a burst dynamic backbone. Promoter regulation enables a promoter at a specific genomic location to effectively move within the integration landscape and "look" like a different site.

To reduce error in correlation times to ~ +/-0.075 h for 12 h signatures, polyclonal data was sub-clustered into 34 groups, each containing ~60 cells. The correlation times for the LTR polyclonal population initially have a strong increasing trend until an abundance cutoff (annotated with grey vertical line in Figure 4A) after which the correlation decreases. Consistent with our other results, here a separate measure of stochastic behavior displays an identical abundance cutoff value in agreement with the two intensity dependent burst domains described in Figure 4. TSA addition yields a significantly different result than the TNF addition with a drastically different molecular mechanism (SI Figure 19). Although its sub-clusters are constrained to the burst dynamic trends as the non-drug case (Figure 4), correlation times fail to decrease in the higher abundance sub-clusters while BS significantly increases. This alludes to BS increasing through increases of k_m as opposed to decreases of k_{off}. This TSA regime of non-kinetic burst size modulation agrees with TSA experiments by Suter *et al* (19). The autocorrelation analysis of time-lapse microscopy data enabled the discrimination between

different modes of transcriptional regulation with drug additions (changes in k_{off} versus k_m) that would not be possible with noise magnitude measurements alone.

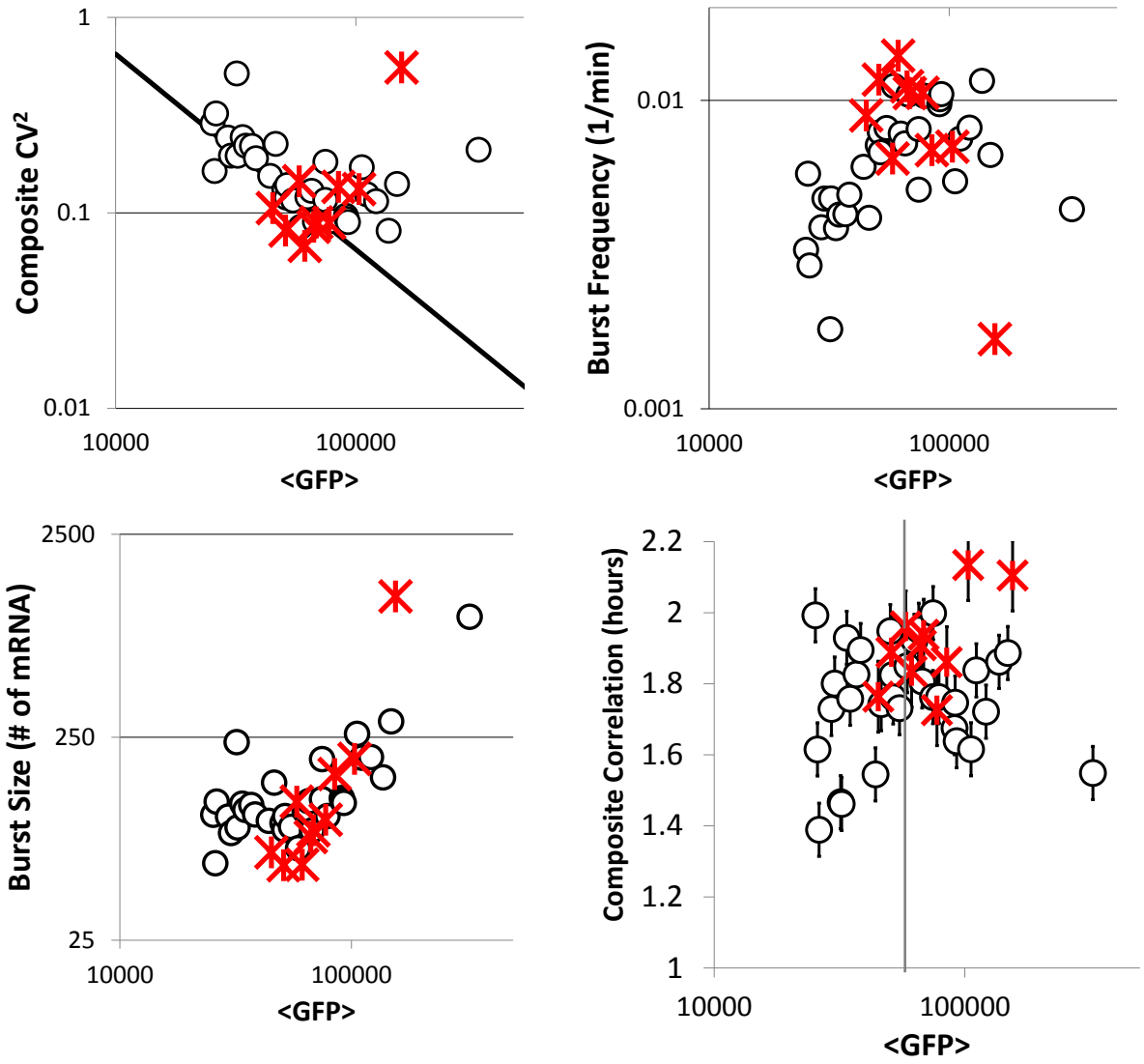

SI Figure 19: Noise and burst trends with TSA addition to the Ld2G poly population.

Short reporter half-lives are required to observe the underlying burst behavior

Theory predicts that a long-lived reporter would "mask" underlying transcriptional bursting (8). Therefore, to study the burst dynamics, it is required that $k_{on} + k_{off}$ is within the same range as the mRNA and protein half-lives. In either extreme, cases of rapid degradation or stability the transcriptional bursting would be difficult to resolve. To demonstrate this, we expressed and performed flow cytometry on 22 isoclonal populations infected with a two-reporter system (LTRd2GFP + LTRmCherry), where the two LTR promoters were integrated at different integration sites. The resulting noise magnitudes demonstrate that the stable mCherry signal does not produce our observed signature of increasing burst size at high protein abundances (SI Figure 20). TNF and TSA addition extend the increased burst size in the GFP case while extending the downward noise magnitude in the mCherry case.

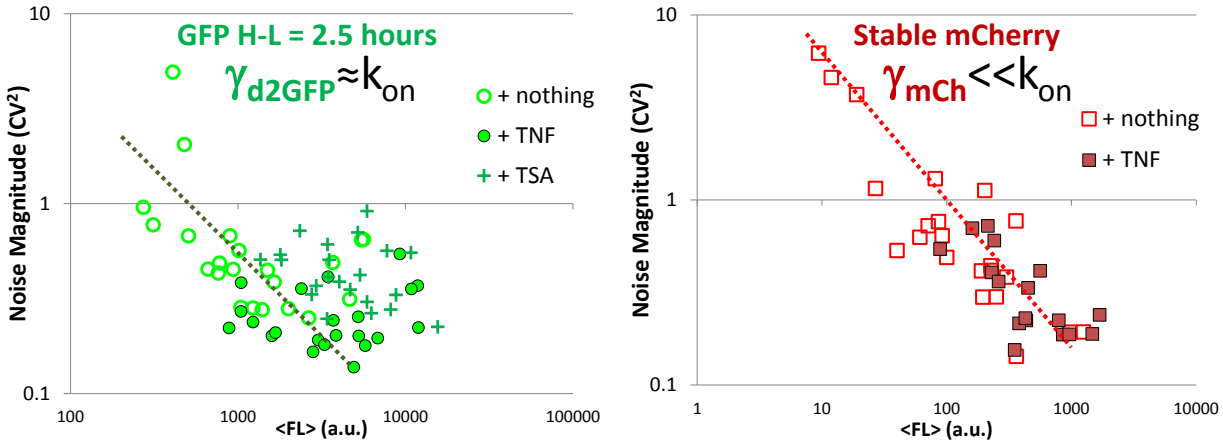

SI Figure 20: (**Left)** Short-lived GFP captures transcriptional burst behavior (**Right)** As predicted by theory (see Equation S-2 and (7, 8)), a stable mCherry reporter masks the underlying burst dynamics.

Gene Expression Distributions and Noise Shift Validation

Mean single-cell intensity distributions for three isoclones and three regions of the LTR polyclonal population were determined and represented with an overlaid gamma-distribution (red curves) (23). Noise magnitude values extracted from the fits are consistent with the autocorrelation-based noise analysis performed in the paper (Figs. 2D, 4C, and S1) and those found by others to quantify noise (23, 24).

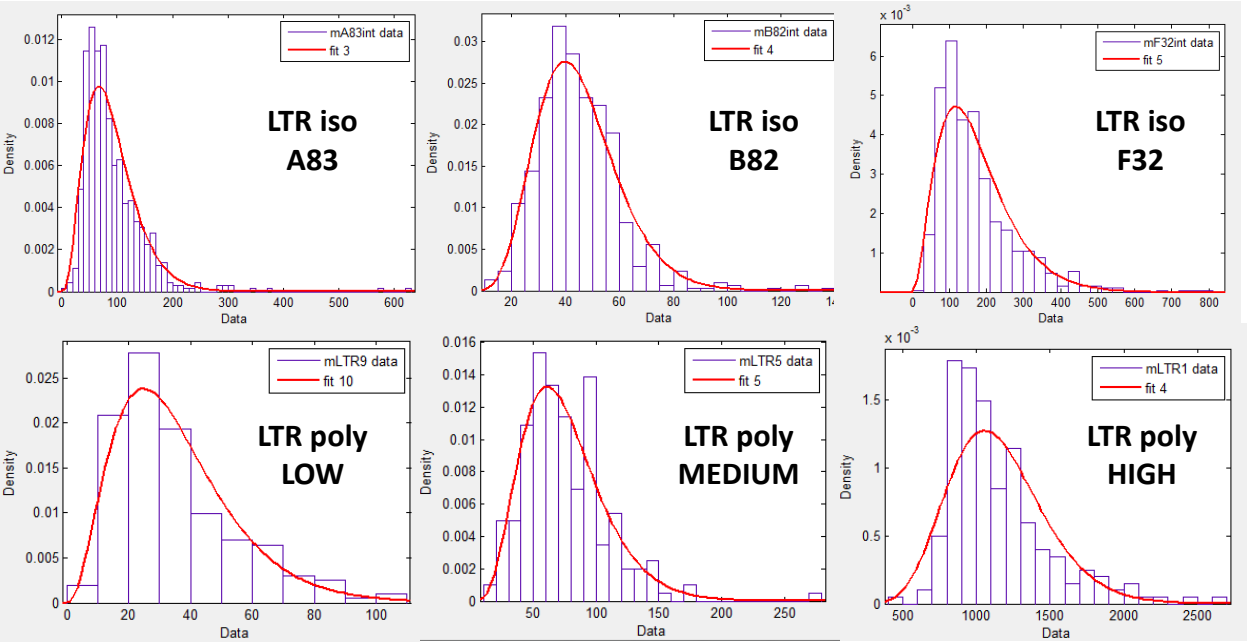

Experiment	Mean	a (shape)	b (scale)	CV^2	FF
A83 iso	90.6393	3.8698	23.4222	0.258411	23.4222
B82 iso	44.8988	8.73762	5.13856	0.114448	5.13856
F32 iso	173.0792	3.07449	56.2954	0.325257	56.2954
LTR poly clust LOW	35.4338	3.35849	10.5505	0.297753	10.5505
LTR poly clust MED	75.0461	5.25513	14.2806	0.19029	14.2806
LTR poly clust HIGH	1148.1	12.4896	91.9263	0.080067	91.9263

SI Figure 21: Gene-expression distributions for LTR isoclones and polyclone sub-clusters along with their gamma-function fit parameters. Distributions of fluorescence intensity (a.u., x-axis) are represented with an overlaid gamma-distribution (red curves) (23), and the resulting parameters agree with calculated autocorrelation-based noise magnitudes in the main text (Figures 2D, 4C, and S1).

Supplementary Figure S1

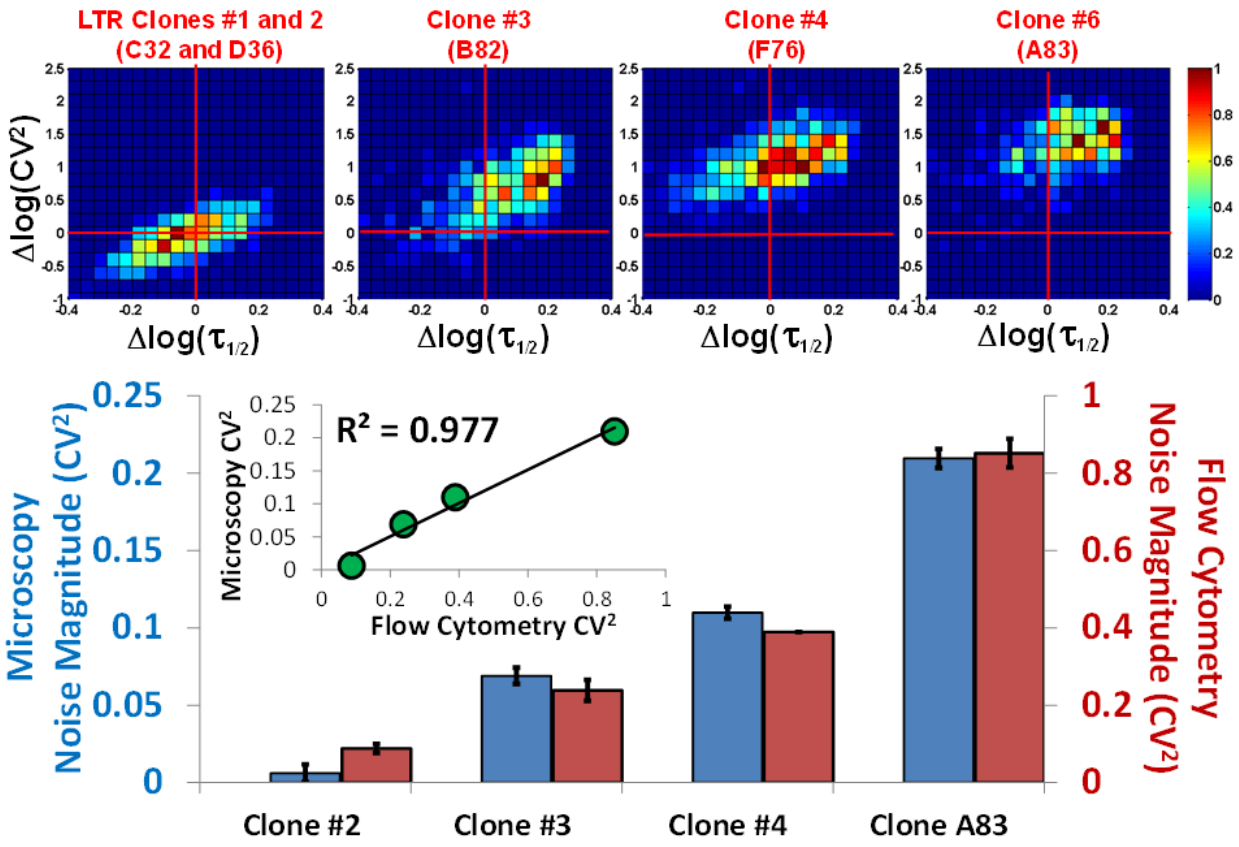

Supplementary Figure S1: Benchmarking and validation of microscopy noise measurements with conventional flow cytometry. Top: microscopy noise maps for four isoclones from 18-h microscopy experiments. Bottom: Comparison of CV^2 from microscopy (blue) to flow cytometry for the same clones (red). Inset: comparison of microscopy to flow cytometry CV's show measurements are consistent with one another to within a constant. High-frequency processing decreases noise magnitude from flow values consistently by ~0.25 for 18 h imaging durations.

Supplementary Figure S2

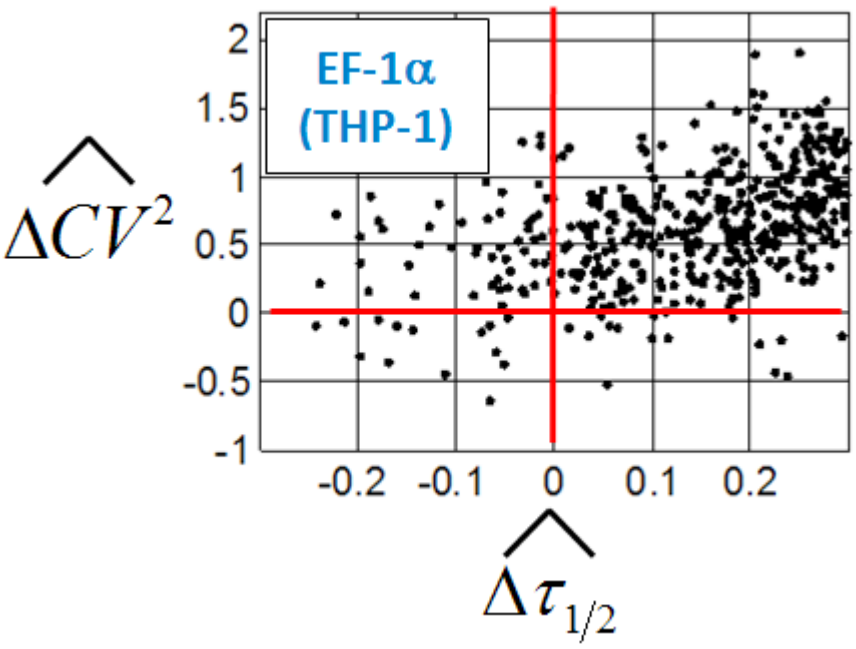

Supplementary Figure S2: Noise-maps for EF-1α promoter in THP-1 cells (a monocyte cell line). Shown is the noise-map scatter plot for ~400 genomic loci and the majority of cells fall in the upper right quadrant of the noise map where signatures dominated by transcriptional bursting are expected to shift.

Supplementary Figure S3

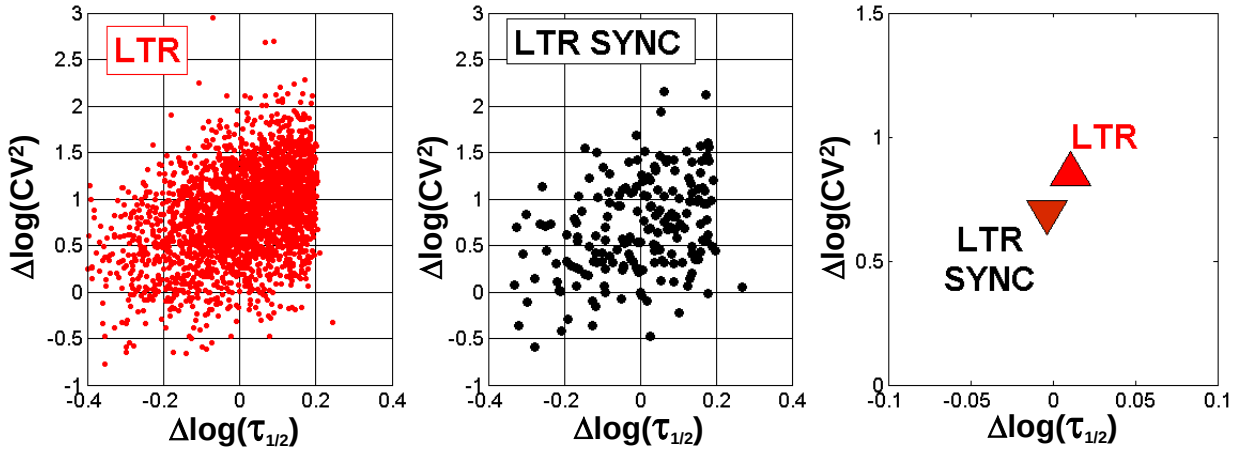

Supplementary Figure S3: Cell-cycle state has little effect on the LTR noise map. Noise-map scatter plots of the unsynchronized LTR-GFP population (left) and a synchronized LTR-GFP population in which ~85-90% of cells are in the G1 phase of cell cycle (center). Both noise maps are shifted into the upper-right quadrant and have very similar noise-map centroids (right).

Supplementary Figure S4

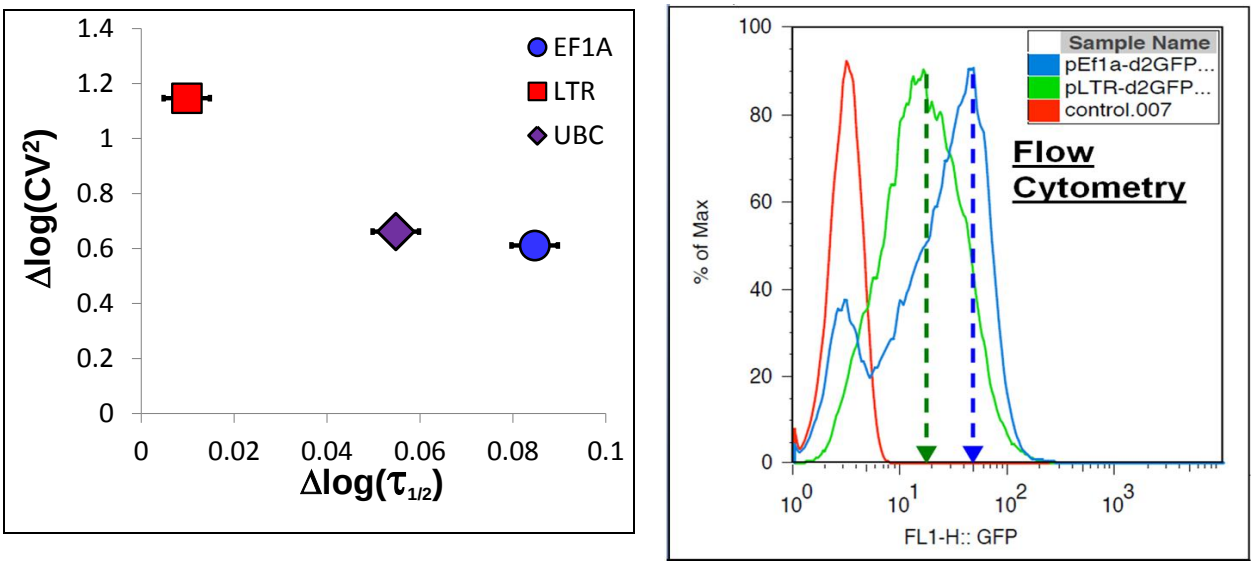

Supplementary Figure S4: The HIV-1 LTR exhibits a greater noise-magnitude shift compared to EF-1α and UBC promoters. (Left) Noise-map centroids for the polyclonal populations of LTR, EF-1α and UBC promoters determined from noise maps in Figure 3 of the main text. The LTR promoter has a higher noise magnitude and decreased correlation shift. The error bars show ± 1 sigma uncertainty in the centroid positions as determined by the number of cells in the sample (SI Figure 14). Noise-map centroids are determined from the base-line in Figure 2D (Clones 1 and 2), (Right) Flow cytometry verification showing distributions for EF1A-d2G (blue) and LTR-d2G (green). $CV_{LTR} > CV_{EF1A}$. The stronger EF1A promoter displays increased mean expression compared tothe HIV-1 LTR, consistent with published findings (25).

Supplementary Figure S5

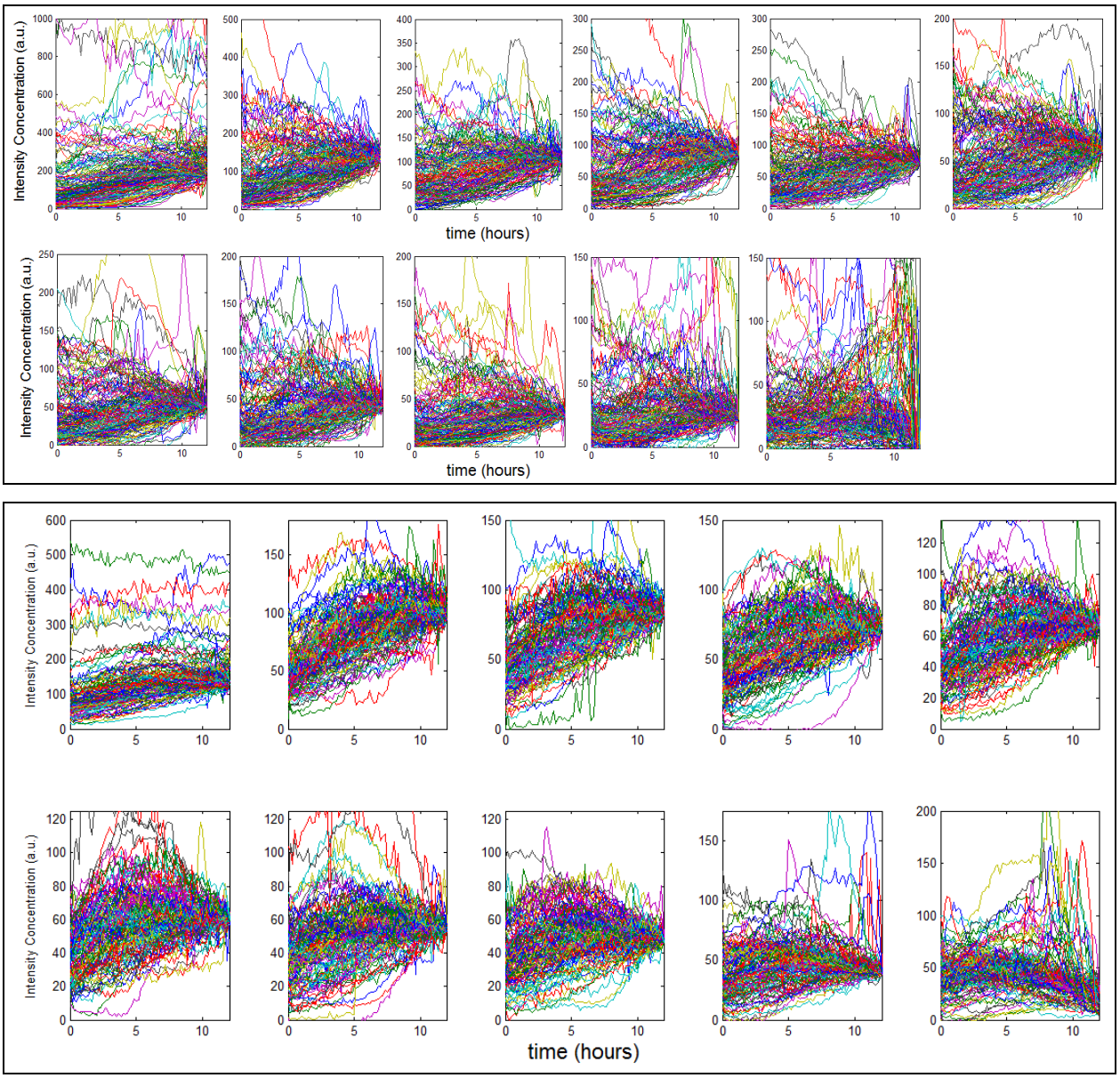

Supplementary Figure S5: Sub-clustered GFP intensity trajectories of polyclonal populations. (Upper) LTR polyclonal cells separated into 11 clusters of 170 cells by their last intensity values. Sub-clusters decrease in intensity from the upper-left to lower-right panels. (Lower) 10 sub-clusters of Ef1A d2GFP poly clustered in the same way as the LTR polyclonal cells. The sub-clustering of the UBC populations is not shown.

Supplementary Figure S6

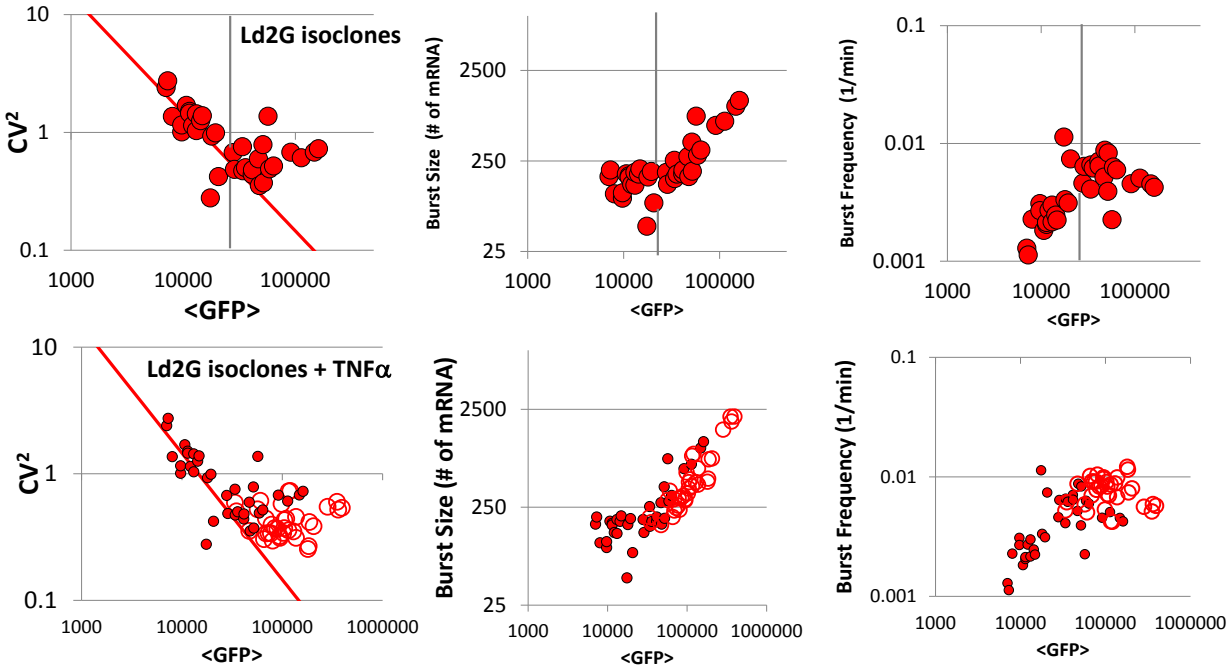

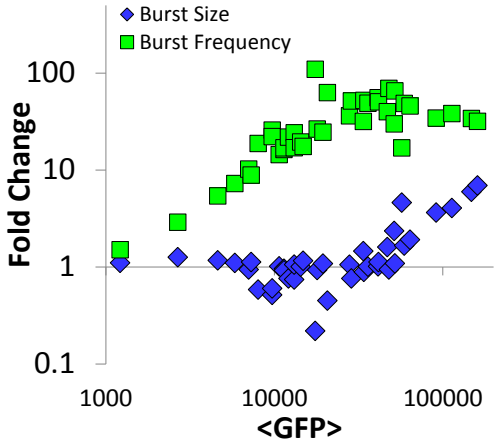

Supplementary Figure S6: LTR isoclones yield similar noise and burst trends to polyclonal sub-cluster processing when measured using traditional flow cytometry methods. 35 Ld2G isoclones were measured for their fluorescence distributions by flow cytometry. The measurements of a range of LTR isoclones yielded noise and burst dynamic trends similar to the polyclonal microscopy data. As described (16), the coefficient of variation squared and mean levels were used to quantify gene expression noise magnitude in the LTR isoclones which generally land along a single burst model line inversely proportional to the fluorescence abundance. Here, deviations from the trend are only observed at high abundances. At low abundances, the burst size remains constant, while the burst frequency increases (left of vertical gray line). At higher abundances, the BF hits an upper bound and plateaus, and abundance

increases through increases in burst size (identical to Figure 4a, right of vertical gray line). Upon TNFα addition (middle row), shifts along the noise and burst trends identical to the polyclonal sub-clusters (Figures 5) are observed. Finally, the fold change in burst size and frequency are comparable to one another and use flow cytometry to support the main text observation that modulations in burst size and frequency are equivalent (Figure 4).

The consistency in noise measurements between the two methods suggests that the high throughput image and signal processing of the genome-wide polyclonal microscopy signatures does not bias or affect the underlying biological general trends while providing a widespread integration dependent picture (Fig. 4B and Supplementary Figures S7 and S8). The polyclonal noise magnitude results are lower than the isoclone values. Finite duration imaging experiments are limited in the variability and correlations they can capture. Imaging experiments capture a high-frequency (HF) portion of the total underlying frequency domain which results in noise magnitudes that are ~30 to 60% of true values for 12-h intensity trajectories (see section above on "Noise map variance dependence on experiment duration"). In addition the sub-clustered polyclonal data aggregate many clones and are therefore less prone to outliers on the extreme ends/tails of the noise magnitude and burst trends compared to the 35 isoclones.

Supplementary Figure S7

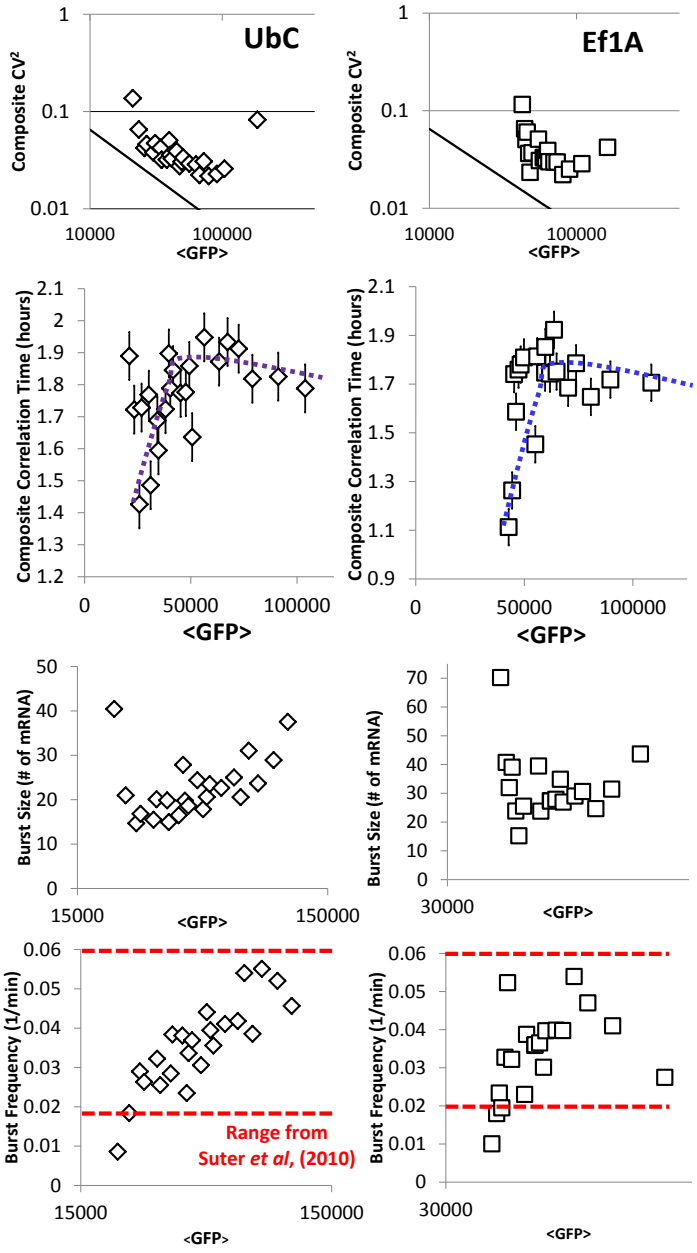

Supplementary Figure S7: Two housekeeping promoters display increasing episodic expression with increasing intensity levels. The 2-state model and burst size expressions predict burst size = 0 for constitutive or continuous gene expression (Equations 1-3 and S-1). If C_1 is constant among all three promoters (a fair assumption since C_1 is a function of g_m, g_p, and k_p), burst size can be calculated. Both UBC and EF1A have markedly less BS than the LTR (LTR starts at ~100 mRNA). Interestingly, the burst frequency range for these two strong promoters are consistent with the range of burst frequencies reported by Suter *et al*., (19), and further emphasizes that each individually span the kinetic range with varying integration site. Although much less bursty than the LTR, both the UBC and EF1A polyclonal sub-clusters have

noise-correlation trends and ranges comparable to the LTR case. The ~0.6-0.7 h shifts at higher intensity values indicate expression that is far from constitutive by both isoclone experiments (Figure 2D) and constitutive simulations (12-h HF-T50 = 1.55 h, SI Figure 4). The increase in correlation time can be explained by burst frequency modulation in the low intensity domain. At higher intensities correlation times are close to constant indicating a pure increase in transcription rate (k_m). In both UBC and EF1A cases, burst size and burst frequency appear to increase in a similar two-domain manner to the LTR and with burst size being increased by k_m at in the higher intensity domain.

SUPPLEMENTARY REFERENCES:

1. Dull T, *et al.* (1998) A third-generation lentivirus vector with a conditional packaging system. *J Virol* 72(11):8463-8471.
2. Weinberger LS, Burnett JC, Toettcher JE, Arkin AP, & Schaffer DV (2005) Stochastic gene expression in a lentiviral positive-feedback loop: HIV-1 Tat fluctuations drive phenotypic diversity. *Cell* 122(2):169-182.
3. Lois C, Hong EJ, Pease S, Brown EJ, & Baltimore D (2002) Germline transmission and tissue-specific expression of transgenes delivered by lentiviral vectors. *Science* 295(5556):868-872.
4. Rinaudo K, *et al.* (2007) A universal RNAi-based logic evaluator that operates in mammalian cells. *Nat Biotechnol* 25(7):795-801.
5. Weinberger LS, Dar RD, & Simpson ML (2008) Transient-mediated fate determination in a transcriptional circuit of HIV. *Nat Genet* 40(4):466-470.
6. Banfalvi G (2008) Cell cycle synchronization of animal cells and nuclei by centrifugal elutriation. *Nat Protoc* 3(4):663-673.
7. Simpson ML, Cox CD, & Sayler GS (2004) Frequency domain chemical Langevin analysis of stochasticity in gene transcriptional regulation. *J. Theor. Biol.* 229(3):383-394.
8. Cox CD, McCollum JM, Allen MS, Dar RD, & Simpson ML (2008) Using noise to probe and characterize gene circuits. *Proc. Natl. Acad. Sci. U. S. A.* 105(31):10809-10814.
9. Weinberger LS, Dar RD, & Simpson ML (2008) Transient-mediated fate determination in a transcriptional circuit of HIV. *Nature Genet.* 40(4):466-470.
10. Austin DW, *et al.* (2006) Gene network shaping of inherent noise spectra. *Nature* 439(7076):608-611.
11. Singh A, Razooky B, Cox CD, Simpson ML, & Weinberger LS (2010) Transcriptional bursting from the HIV-1 promoter is a significant source of stochastic noise in HIV-1 gene expression. *Biophys J* 98(8):L32-34.
12. Li XQ, *et al.* (1998) Generation of destabilized green fluorescent protein transcription reporter. *J Biol Chem* 273(52):34970-34975.
13. Raj A, Peskin CS, Tranchina D, Vargas DY, & Tyagi S (2006) Stochastic mRNA synthesis in mammalian cells. *Plos Biol* 4(10):1707-1719.
14. Jordan A, Defechereux P, & Verdin E (2001) The site of HIV-1 integration in the human genome determines basal transcriptional activity and response to Tat transactivation. *Embo J* 20(7):1726-1738.
15. Walters MC, *et al.* (1995) Enhancers increase the probability but not the level of gene expression. *Proc Natl Acad Sci U S A* 92(15):7125-7129.
16. Singh A, Razooky B, Cox CD, Simpson ML, & Weinberger LS (2010) Transcriptional Bursting from the HIV-1 Promoter Is a Significant Source of Stochastic Noise in HIV-1 Gene Expression. *Biophys J* 98(8):L32-L34.
17. Schwanhausser B, *et al.* (2011) Global quantification of mammalian gene expression control. *Nature* 473(7347):337-342.
18. Sharova LV, *et al.* (2009) Database for mRNA half-life of 19 977 genes obtained by DNA microarray analysis of pluripotent and differentiating mouse embryonic stem cells. *DNA Res* 16(1):45-58.
19. Suter DM, *et al.* (2011) Mammalian genes are transcribed with widely different bursting kinetics. *Science* 332(6028):472-474.

20. Raj A, Peskin CS, Tranchina D, Vargas DY, & Tyagi S (2006) Stochastic mRNA synthesis in mammalian cells. *PLoS Biol* 4(10):e309.
21. Schroder AR, *et al.* (2002) HIV-1 integration in the human genome favors active genes and local hotspots. *Cell* 110(4):521-529.
22. Elowitz MB, Levine AJ, Siggia ED, & Swain PS (2002) Stochastic gene expression in a single cell. *Science* 297(5584):1183-1186.
23. Friedman N, Cai L, & Xie XS (2006) Linking stochastic dynamics to population distribution: an analytical framework of gene expression. *Phys Rev Lett* 97(16):168302.
24. Taniguchi Y, *et al.* (2010) Quantifying E-coli Proteome and Transcriptome with Single-Molecule Sensitivity in Single Cells. *Science* 329(5991):533-538.
25. Weinberger LS & Shenk T (2007) An HIV feedback resistor: auto-regulatory circuit deactivator and noise buffer. *PLoS Biol* 5(1):e9.